Neutral hydrogen in the archetype post-merger, dual active galactic nucleus system NGC 6240

By

Karina Caitlin SANTANA

UNIVERSITEIT VAN PRETORIA
UNIVERSITY OF PRETORIA
YUNIBESITHI YA PRETORIA
Denkleiers • Leading Minds • Dikgopolo tša Dihlalefi

Department of Physics
UNIVERSITY OF PRETORIA

Submitted in partial fulfilment of the requirements for the degree of MASTER OF SCIENCE (MSC) IN PHYSICS in the Faculty of Natural and Agricultural Sciences.

October 7, 2022

Supervisor: Prof. Roger DEANE

UNIVERSITY OF PRETORIA

Abstract

Faculty of Natural and Agricultural Sciences
Department of Physics

Master of Science (MSc) in Physics

Neutral hydrogen in the archetype post-merger, dual active galactic nucleus system NGC 6240

by Karina Caitlin SANTANA

Supervisor: Prof. Roger DEANE

NGC 6240 is a prototypical merger system in the nearby universe hosting a dual active galactic nucleus. It is a well studied object and has been observed across the electromagnetic spectrum using most major ground- and space-based observatories over several decades. In this thesis, we report on the first detection of H I emission in this system. We find that there are two planes of H I emission, one aligned with the galactic dust plane and the other in line with a neighbouring galaxy at a projected separation of $\sim$90 kpc. This interacting neighbour has extended ultraviolet and compact x-ray emission, indicating active star formation and active nuclear black hole accretion, respectively. As far as we are aware, this is the first evidence of an interaction between NGC 6240 and this neighbouring galaxy. Overall, the H I emission is predominately found to the south of the dual AGN, including some tidal debris to the south-west. The previously reported H I absorption is shown to have the same orientation as the galaxy disk, based on the high-imaging fidelity and sensitivity, which enable high relative astrometry of the absorption line. Combining the above, we are able to compare and contrast the H I emission and absorption view, providing a richer picture of this prototypical local-universe merger system. Detailed H I studies such as this will improve our understanding of H I at galaxy formation and evolution in higher redshift systems, where the galaxy merger rate, AGN prevalence, and cosmic star formation rate density all show a dramatic increase.

Declaration of Authorship

I, Karina Caitlin SANTANA, declare that the thesis, which I hereby submit for the degree of MSc in Physics at the University of Pretoria, is my own work and has not previously been submitted by me for a degree at this or any other tertiary institution.

Signature: 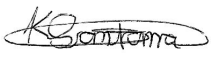

Date: 1/08/2022

"A bit of science distances one from God, but much science nears one to Him... The more I study nature, the more I stand amazed at the work of the creator."

Louis Pasteur

Acknowledgements

This degree has been a unique experience I am so grateful to have had. Completing this degree during a global pandemic had many challenges; working from home, isolation from colleagues and friends, loss of loved ones and uncertainties around "normal" life returning. I have grown during this experience and would not have made it without the support and guidance from people throughout my degree.

To my supervisor, Prof Roger Deane. Thank you for your guidance and understanding throughout my degree. Thank you for flaming my passion for radio astronomy and assigning me this exciting project. Thank you for your encouragement and for teaching me so much. You are a big inspiration, and I look forward to learning from and working with you again.

To Leon, thanks for the phone calls during lockdown and lengthy discussion on our projects and life in general. It has been amazing doing radio astronomy and SARAO related activities with you, thanks for being a great friend and colleague these past few years.

To my UP colleagues, Shilpa, Paul, Heinrich and Isaac. Thank you for the insightful discussions and for being available and willing to help. To Jack and Kshitij, thank you for your optimism and reassurance. I enjoyed our conversations and getting to know you both.

A big thank you to my friend group that grew closer during the pandemic. Thanks to Megan and Bevan for organising zoom game evenings to keep us all connected. Thanks to Rachel, Lisa, Paul and Nicolas for organising activities and hikes that kept me sane and active. These past two years, we have faced many challenges with covid and the losing loved ones, which I would not have gotten through without you. Words cannot express how much I appreciate all your support and love through the good and the bad.

To my mom. Thank you for supporting me in everything I do. Thank you for comforting me during the heartbreaks and being my biggest cheerleader. To my little sister, thank you for being an epic office mate, for making me laugh (and also making me crazy). To my gran, thank you for all the food and Sunday gatherings during lockdown, it was the highlight of every week. I love you all so much and would not have come this far without you.

To Ruan. Thank you for being there in these final few months. Thank you for always having a shoulder to cry on and reassurance when I doubt myself. I cannot help but feel joy with you around. I appreciate your love and support lots.

The financial assistance of the South African Radio Astronomy Observatory (SARAO) towards this research is hereby acknowledged (www.sarao.ac.za). We acknowledge the use of the ilifu cloud computing facility (www.ilifu.ac.za). This work made use of the CARTA (Cube Analysis and Rendering Tool for Astronomy) software (DOI 10.5281/zenodo.3377984 - https://cartavis.github.io). The data used was from MeerKAT telescope observations. The MeerKAT telescope is operated by the South African Radio Astronomy Observatory, which is a facility of the National Research Foundation, an agency of the Department of Science and Innovation.

Contents

List of Figures

List of Tables

Chapter 1

Introduction

1.1 Galaxy formation and evolution

How galaxies form and evolve is one of the biggest questions astronomers try to solve. Cold dark matter, ΛCDM, cosmology is the most popular/accepted theory, currently explaining galaxy formation as "outside in". This theory explains that from the Big Bang onward, baryonic matter collapse along with dark matter, forming large-scale structure, galaxies and stars (Péroux and Howk, 2020). A minority of baryonic matter is found in stars, even 13.7 Gyrs after the Big Bang. Over 90 % of baryons in the universe are still found in the gaseous phase. The cold component of that gas, traced by H I and H_2, provides fuel for star formation (Péroux and Howk, 2020).

The galaxy population at low redshifts can be split into two groups, blue and red, defined by the structure, stellar content and chemical composition of the galaxy (Heckman and Best, 2014). The galaxies found in the blue population (late Hubble type) have significant on-going star-formation (0.1 Gyr^{-1}), and lower stellar mass $M_\star$ (10^{10} $M_\odot$), with an almost linear relationship between star-formation rate and $M_\star$. This relationship is now known as the star-forming main sequence. The galaxies in the blue population also have low stellar surface mass density and small concentrations of their light, defined by $\mu_\star = 0.5\ M_\star/(\pi R_{50}^2)$ and $C = R_{90}/R_{50}$ respectively (Heckman and Best, 2014). On the other hand, the galaxies defined as the red population (early Hubble type) are the opposite, with little on-going star formation, large $M_\star$, large C and high $\mu_\star$. The transitions between the two populations are marked by the following values for each parameter: $M_\star \sim 10^{10.5}$ $M_\odot$, $\mu_\star \sim 10^8.5$ $M_\odot$ kpc^{-2} and C $\sim$ 2.6 (Heckman and Best, 2014). The relationship between $M_\star$ and specific star formation rate, sSFR, for galaxies at low redshifts, $z < 2$, is shown in figure 1.1, where sSFR = SFR/$M_\star$. This image is taken from Heckman and Best (2014), where they used the main galaxy sample from the Sloan Digital Sky Survey (SDSS) Strauss et al. (2002). The main takeaway from the plot is that the sSFR values, along the star forming main sequence, change significantly with time (Heckman and Best, 2014).

The evolution of a typical galaxy can be simplified as follows. The galaxy evolves along the rapidly evolving blue, star-forming, main sequence. Here the galaxy mass increases by the accretion of cold gas from the cosmic web or by mergers with other galaxies. The mass approaches a critical mass where its supply of cold gas is halted and the star formation is quenched. The galaxy has now evolved into the red population. The mass of the galaxies can still increase through mergers with other galaxies (Heckman and Best, 2014). At the centre of most large galaxies is a super massive black hole (SMBH) with size of order 10^{6-10} $M_\odot$ (Urry, 2003).

Many processes could quench star formation, one of which is the heating and the ejection of gas surrounding an Active Galactic Nuclei (AGN) by AGN-driven outflows, known as AGN feedback. An AGN is a super massive black hole that is

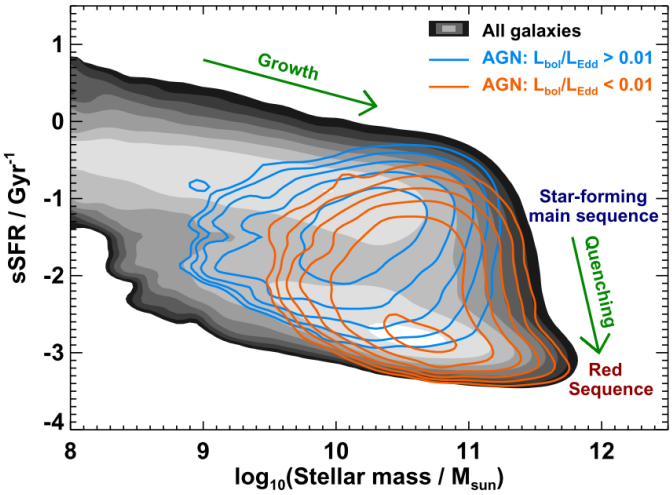

FIGURE 1.1: The Sloan Digital Sky Survey (SDSS) main galaxy sample distribution on the plane of stellar mass against specific star formation rate (sSFR = SFR/$M_\star$). The volume-weighted distribution of all galaxies is given by the grey-scale with each lighter colour band increasing by a factor of two. The majority of galaxies can be categorised as star-forming galaxies ('main sequence') or 'quenched' galaxies ('red sequence'). The blue and red contours show the volume-weighted distributions of high and low Eddington-fraction AGN, respectively. The contours are spaced by a factor of two, with blue showing the mostly radiative-mode AGN and red the mostly jet-mode AGN. Image credit: Heckman and Best (2014).

actively accreting matter. In the red/dead population, star formation by the slow accretion of their hot halo gas, can be prevented by AGN feedback. Therefore in the current model and understanding of galaxy evolution, it is clear that AGN and mergers play a crucial role (Heckman and Best, 2014). AGN feedback is only favoured for massive galaxies and for lower mass systems star formation feedback is favoured (Lagos, Cora, and Padilla, 2008).

It is worth noting that not all AGNs result from mergers, there are low level activities in objects such as Seyfert galaxies that appear undisturbed. These objects have other processes occurring and different modes of fuelling that are more significant (Hopkins et al., 2008).

Heckman and Best (2014) go on to say that in the contemporary universe majority of the AGN activity appears to occur without major mergers or strong tidal interactions. A large supply of dense gas in the centre of a galaxy is all that is required regardless of the origin (Heckman and Best, 2014).

1.1.1 Active galactic nuclei (AGN)

To better understand galaxy evolution, we need to understand and study AGN feedback. This is a self-regulating process linking energy released by the AGN to the gaseous medium surrounding the AGN and throughout the galaxy. Active SMBH releases large amounts of energy through jets and outflows, impacting the evolution of their host galaxies. The feedback from AGN is star formation quenching, negative feedback, through two modes, quasar (or radiative) mode and jet (kinetic or mechanical) mode (Morganti, 2017).

In the quasar mode, most of the energy is released by radiation or wind from the accretion disk. This kind of energy release drives outflows, expelling gas from the galaxy and is usually associated with high luminosity AGN (Morganti, 2017).

Jet mode feedback is more common in low-power AGN, where the main source of energy is provided by relativistic jets launched in the vicinity of the nuclear black hole and seen prominently at radio wavelengths. This prevents the cooling of the surrounding gas back into the galaxy(Morganti, 2017).

It is not always easy to differentiate between the modes, and often multi- wavelength observations are required to do so. In a review by Heckman and Best (2014), they differentiate between the two types of AGN in terms of the properties of their SMBH and host galaxies, shown in the schematic drawings in Figure 1.2.

The radiative mode AGN consists of objects with a dominant energetic output in the form of electromagnetic radiation, which is produced by efficiently converting the potential energy of the SMBH's accreted gas. These are well known as Seyfert galaxies or QSOs, which used to depend on a variety of criteria of luminosity and viewing angle. The left panel of figure 1.2 is the schematic drawing of the central engine for radiative mode AGN showing that in the stable innermost orbit around the SMBH, there is a geometrically-thin and optically-thick accretion disk. The broad line and narrow line region is illuminated by ultraviolet radiation from this accretion disk (Heckman and Best, 2014). A dusty, toroidal-like structure can obscure the view of the accretion disk and broad line region when viewed near the equatorial plane (type 2). When viewed near the polar axis, type 1, the accretion disk and broad line region is visible.

This obscuring material is large-scale dusty interstellar medium of the host galaxy at an inclination and is relevant when viewing the disk of the host galaxy or a gas and dust-rich system with a lot of clear extinction, the characterisation of which is complicated by merger-induced disruption of a system.

This material is able to obscure the AGN's optical, UV, and soft x-ray but not hard x-ray emission from the accretion disk and broad line region (Heckman and Best, 2014).

Jet mode AGN objects produce little radiation where the majority of the energy is released by kinetic energy through a collimated jet outflow in two directions. These jets are powered either by the accretion of gas or through the spin energy of the SMBH (Heckman and Best, 2014). The galaxies in this population are commonly known as low-excitation radio galaxies. The right panel of figure 1.2 is the schematic drawing of jet mode AGN. Near the inner regions, close to the SMBH, the accretion disk is either optically thin or truncated, and instead, there is an advection-dominated accretion flow structure which is geometrically-thick. In this structure, the inflow time is shorter than the radiative cooling time, making them capable of launching two-sided jets. These jets are detected via synchrotron emission produced at radio wavelengths and can extend far past the stellar body of the galaxy travelling at relativistic velocities when launched. The jets remain highly collimated until they are terminated by interacting with inter-galactic medium, creating bright shocks/hot spots. There may be a transition to a truncated outer thin disk for AGN with larger radii. The weak narrow line region can be ionized by less powerful radiative emission, especially when the radius of the truncated thin disk is low (Heckman and Best, 2014).

Synchrotron emission is produced by the acceleration of charged particles around a magnetic field and is the main mechanism for radiation in AGN, observable across the electromagnetic spectrum. However, accretion disk gas is heated like a black body and the thermal peak shifts to ultra-Violet wavelengths (Urry, 2003).

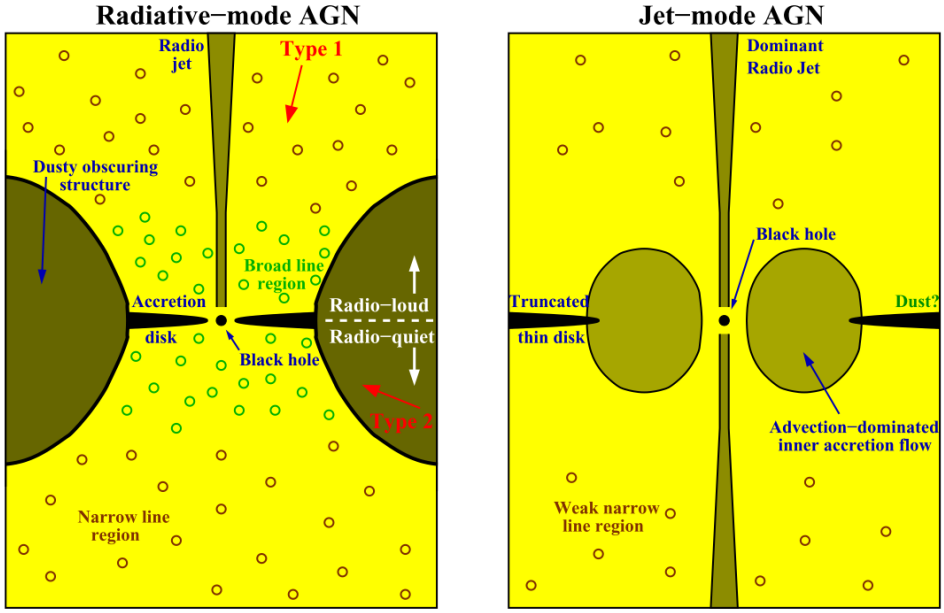

FIGURE 1.2: Schematic drawing of the two types of AGN described by Heckman and Best (2014), namely radiative-mode (left panel) and jet-mode (right panel) AGN. Image credit: Heckman and Best (2014)

1.1.2 Star formation feedback

Star formation feedback, also known as stellar feedback, involves the expelling and transferring matter, momentum and energy from a star into the surrounding interstellar medium (ISM). Large OB-type stars dominate the lower-mass stars, in importance of stellar feedback in terms of; material, momentum and energy emitted per star. Feedback in the form of jets, conversion of gravitational potential energy to heat, are dominant in low- and intermediate-mass stars, usually found in clouds without O-type stars. These clouds are usually small and cannot support large star formation or have not had enough time to form O-type stars (Dale, 2015).

Mass-loaded kinetic energy from stars is the kinetic energy from supernova ejecta and stellar winds. This energy is effectively injected into the ISM, which affects the gas properties and star formation in galaxies (Mo, van den Bosch, and White, 2010).

Stellar Winds - During the late evolutionary stages of stars, it is possible for some stars to lose large amounts of their mass through stellar winds (Mo, van den Bosch, and White, 2010). These winds are powerful fluxes of energetic photons which are emitted by OB stars. Material from a main-sequence O-type stars' surface is expelled at velocities of order 10^3 km s^{-1}, which is approaching the wind terminal velocity, v_∞ (Dale, 2015).

Supernova Explosions - Massive stars with mass > 8 M$_\odot$ eventually exhaust their core hydrogen resulting in a chain of events ending in a supernova explosion. These explosions causes an ejection of ~ 10 M$_\odot$ of material at speeds of $\approx 3 \times 10^3$ km s^{-1} (Dale, 2015). Supernova and stellar winds shock the gas, heating it to high temperatures which create bubbles and filaments of hot gas (Hopkins, Quataert, and Murray, 2012).

1.1.3 Galaxy mergers

As mentioned, galaxy mergers play a large role in galaxy evolution and SMBH growth. Strong tidal interactions during mergers can trigger AGN formation and starburst in galaxies. Mergers trigger star formation, SMBH growth and gas outflows.

There have been many attempts to quantify the frequency of galaxy-galaxy mergers, merger rates. Merger rate can depend on multiple parameters such as progenitor masses, redshift and gas fractions. Simulations performed in Lotz et al. (2011) found that the different ranges of mass ratio created a significant difference in merger rates. They also found that major merger rates, with constant number density, evolves strongly with redshift.

Rodriguez-Gomez et al. (2015) found a single fitting function for galaxy-galaxy merger rate. For medium-sized galaxies ($M_\star \gtrsim 10^{10}$ M$_\odot$), this function remained accurate over a range of stellar masses, progenitor mass and redshift. This function is illustrated in figure 1.3, which clearly shows how the merger rate increases with increasing redshift Rodriguez-Gomez et al. (2015).

Mergers trigger star formation due to the disruptions of angular momentum and subsequent inward collapsing of gas. Figure 1.4 from Madau and Dickinson (2014) shows star formation rate as a function of redshift for data from a deep survey of various wavelengths. It is clear from this plot that SFR increases significantly with redshift. This is similar to the trend seen with the merger rate. SFR density peaked at $z \approx 1.9$, about 3.5 Gyr after the Big Bang, then declined exponentially (Madau and Dickinson, 2014).

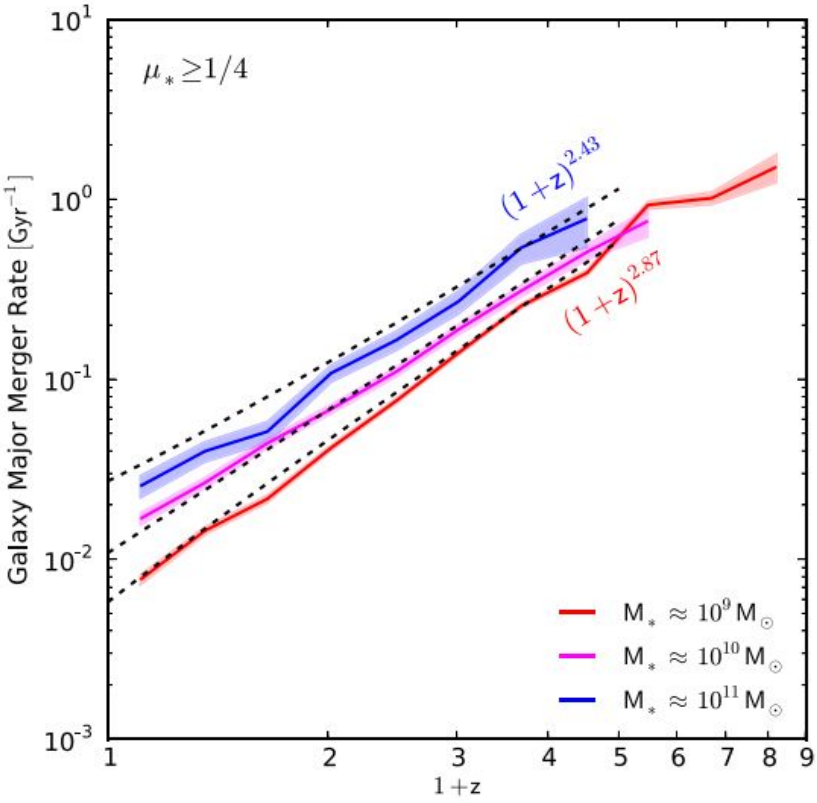

FIGURE 1.3: Merger rate as a function or redshift shown for different descendant masses, blue, pink and red lines with shaded region the Poisson noise. μ_* is the progenitor stellar mass ratio. The fitting function from Rodriguez-Gomez et al. (2015) is integrated over a mass ratio interval, represented by the black dashed line. Image credit: Rodriguez-Gomez et al. (2015)

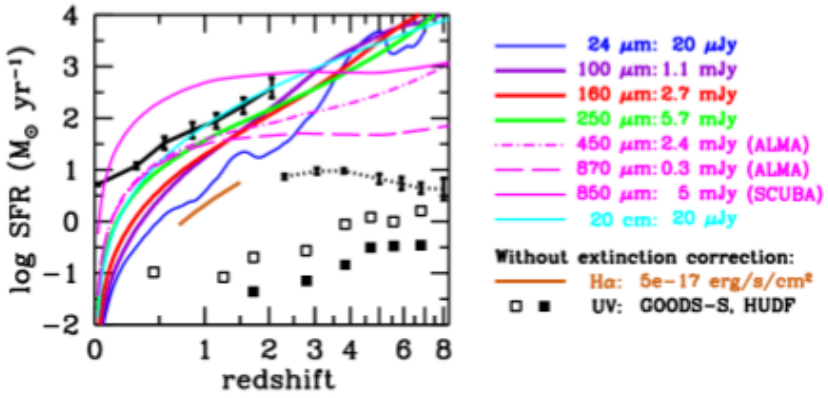

FIGURE 1.4: Sensitivity to SFR as a function of redshift for deep survey data at multiple wavelengths. The wavelengths and corresponding flux limits is shown in the key on the right. Image credit: Madau and Dickinson (2014)

An extreme example of this increased star formation rate is seen in the class of UltraLuminous Infrared Galaxies (ULIRGs), thought to be caused by the merging of two gas-rich spiral galaxies. Solomon and Bout (2005) compare ULIRGs and Early Universe Molecular Emission Line Galaxies (EMGs), or submillimetre galaxies. Both of these classes have high luminosity ($> 10^{12}$ $L_\odot$), average gas mass $\sim 7 \times 10^9 M_\odot$ and a central rotating disk of concentrated molecular gas of 0.7-2.5 kpc in diameter. Both submillimetre galaxies and ULIRGs have very large gas line widths, which correspond to very disrupted gas related to merger dynamics (Solomon and Bout, 2005). However EMGs may have higher SFR and higher molecular gas which suggests that a portion of this submillimetre population represents the formation of giant elliptical galaxies, which is not similar to ULIRGs.

The classical picture of galaxy and black hole co-evolution postulates that SMBHs grow in the aftermath of a major merger and feedback from the growing black hole blows away remaining gas, as discussed and simulated in Hopkins et al. (2006b).

Hopkins et al. (2008) define two criteria for galaxy mergers to occur regarding halo mass, $M_{\rm halo}$. Firstly the halo needs to host a minimum of two galaxies with similar mass, $\sim M_{\rm gal}$. The second criterion is that the merger must be efficient, occurring in much less than a Hubble time, $t = 1/H_0 \sim 13.8$ Gyr. For this to occur the mass of the galaxies and their dark matter subhalos must be comparable to the parent halo mass. For example $M_{\rm halo}/M_{\rm gal} \ll 30$ (Hopkins et al., 2008). The timescale for galaxy mergers are shortest when they are large in mass in comparison to their host halo mass which we expect when considering dynamical friction.

Hopkins et al. (2008) model mergers of gas-rich galaxies with distinct phases through which they evolve in hydro-dynamical simulations designed to investigate feedback. The schematic outline of these phases are presented in figure 1.5. First is an isolated disk where the halo and disk grow and most of the stars are formed. Here the galactic disk grows in quiescence until the commencement of a major merger. The majority of Seyfert and low-luminosity quasars arise from this evolution. Isolated disks then get closer to each other creating "Small Groups" and slowly start interacting/merging until final coalescence.

The merging of two galaxies will result in dual SMBH with black hole separations of one to ten kiloparsecs (Urry, 2003). The dual SMBH will eventually sink into the centre of the merger emitting gravitational waves and coalesce. Mergers trigger star-formation, growth of SMHBs and gas outflows which regulate the stellar content (Müller-Sánchez et al., 2018).

During the galaxies final coalescence, strong starbursts are triggered from the massive inflows of gas. The strength of these starbursts are similar to those found in ULIRGs (ultra-luminous infrared galaxies) and SMG (submillimetre galaxies). However in general, the stellar mass formed from these bursts is small in comparison to the contribution of stellar mass of the merging disk. Rapid black hole growth is fed by the high gas densities. Gas and dust obscure the black holes at optical wavelengths. At high redshifts ($z \sim 2$) these heavily obscured black hole growth in a ULIRG stage, predominantly merging binary black holes, dominates the obscured luminous quasar population (Hopkins et al., 2008).

Eventually supernovae and black hole feedback starts to disperse the residual nuclear gas. This transition phase is called the "blowout" and is associated with dust-reddened and/or IR-luminous quasars. The quasar continues to decay until it has become an elliptical galaxy.

In the middle panel of figure 1.5 is the SFR and luminosity during the merger timeline. The SFR starts off high, then has a small peak at the beginning of the interaction and a large peaks around the coalescence/ULIRG phase and "blow out"

phases, followed by a drastic decrease in SFR. Similarly, AGN luminosity also has two peaks during the same phases as SFR peaks, which we expected (Hopkins et al., 2008).

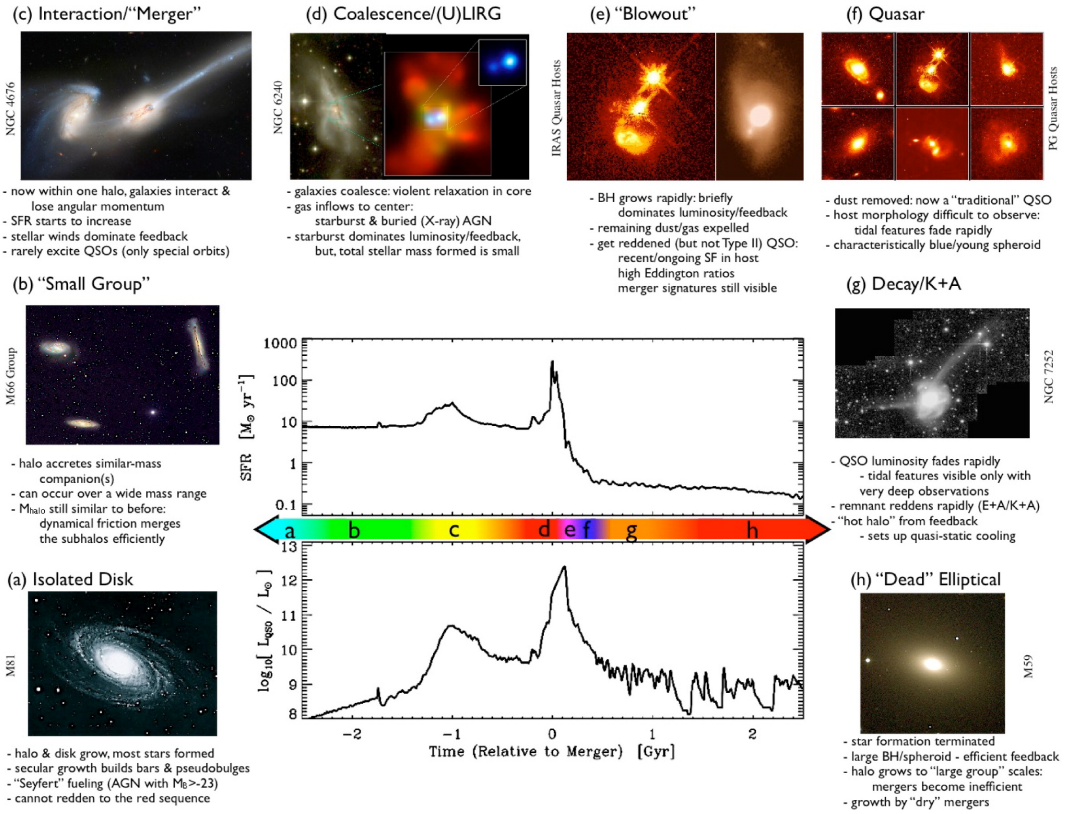

FIGURE 1.5: A schematic outline, taken from Hopkins et al. (2008), of an "ordinary" galaxy going through the phases of growth during a gas-rich major merger. The two plots show how SFR and AGN luminosity changes at different merger phases. Both SFR and luminosity peak around coalescence and the "blowout" phase. Image credits in Hopkins et al. (2008)

1.2 Radio astronomy

In radio astronomy, we study the natural radio emission from celestial objects. Atmospheric opacity and quantum noise in amplifiers define the range of radio frequencies or wavelengths we are able to observe. The upper frequency boundary between radio and far-infrared astronomy is $v \sim 1$ THz (1 THz $\equiv 10^{12}$ Hz), this corresponds to a wavelength $\lambda = c/v \sim 0.3$ mm, where $c \approx 3 \times 10^8$ m s^{-1} is the speed of light in a vacuum. The lower boundary for radio frequency is set by the Earth's ionosphere for ground-based radio astronomy. Extraterrestrial radio waves with frequencies less than $v \sim 10$ MHz ($\lambda \sim 30$ m) are reflected by the Earth's ionosphere, and frequencies less than $v \sim 2$ MHz are absorbed by the ionised interstellar medium in our Galaxy, the Milky Way. These low frequency, v, photons have low energy, E, since $E = hv$ (Condon and Ransom, 2016). Radio telescopes need to be extremely sensitive to be able to detect the radiation. Figure 1.6 shows the atmospheric windows in which ground-based astronomy is confined (Condon and Ransom, 2016).

Radio waves at some level are emitted by almost everything through a large variety of emission mechanisms. Radio waves penetrate interstellar dust clouds and Compton-thick layers of neutral gas; hence few astronomical radio sources are obscured at these wavelengths (Condon and Ransom, 2016).

Radio waves emitted from celestial objects can be detected on Earth by radio telescopes. The majority of radio sources are invariant with time on the scale of minutes or hours, with the exception of pulsars, for example. A large number of emission mechanisms generate photons in a wide range of frequencies in the radio band, which allows a large variety of objects to be observed (Thompson, Moran, and Swenson, 2017).

Synchrotron emission is one of the mechanisms in which radiation is generated; it occurs when high-energy electrons are accelerated in a magnetic field and radiate due to their orbital motion (Thompson, Moran, and Swenson, 2017). Low frequencies are dominated by synchrotron emission. Emission from hot dust grains dominates higher frequencies. These dust grains reach a temperature of about 45K. Gas ionised by central star radiation is often seen in a planetary nebula. This is a thermal radio emission process due to electrons and ions in the plasma, interacting through free-free collisions (Thompson, Moran, and Swenson, 2017).

Electron energies which are distributed continuously, result in a continuum radio spectrum. Continuum radiation is of the most powerful form of radiation with gradual frequency variation along the power spectrum. In contrast, spectral line radiation is created by atomic and molecular processes at specific frequencies. Neutral hydrogen, as discussed in section 1.3, is one of the fundamentally important lines (Thompson, Moran, and Swenson, 2017).

Radio astronomy is responsible for the discovery of a variety of objects and phenomena studied in modern astronomy and cosmology, such as the cosmic microwave background (CMB), quasars, pulsars, indirect evidence of gravitational waves, cosmic magnetic fields, non-thermal emission mechanisms (synchrotron radiation) and jets from black holes (Lazio et al., 2014).

In addition, aperture synthesis techniques have facilitated radio observations to reach remarkable imaging resolutions and precision, which are not reached in other wavelength bands (Lazio et al., 2014).

The international activity of radio astronomy spans most of the available parameter space for observations at radio wavelengths. Due to a variety of radio telescopes, we now have access to a range of frequencies, starting as low as $\sim$ 10 MHz ($\sim$ 30 m), at the ionospheric cut-off to as high as $\sim$ 1 THz ($\sim$ 0.3 mm), corresponding to LOFAR (Haarlem et al., 2013) and ALMA (Stoehr et al., 2014) arrays respectively. Aperture radio telescopes provide good surface brightness sensitivity as well as interferometers using techniques of very long baseline interferometry (VLBI) to achieve sub-milliarcsecond resolutions. See chapter 2.1 for more information regarding radio interferometry.

Significant expansions in one or more directions in the parameter space will be applied to future instruments such as the Square Kilometre Array (SKA). The SKA will be the worlds largest radio telescope operating over a wide range of frequencies and with greater sensitivity than any current radio telescopes (Bull et al., 2020).

Spectral-line radio astronomy started with the first observation of the 21 cm neutral hydrogen (H I) line by Harold Ewen and Edward M. Purcell in 1951, at Harvard (Ewen and Purcell, 1951). In this thesis we use spectral-line radio astronomy to study the neutral hydrogen in a galaxy merger, made possible by a sensitive ground based radio telescope, MeerKAT, discussed later in section 2.2.

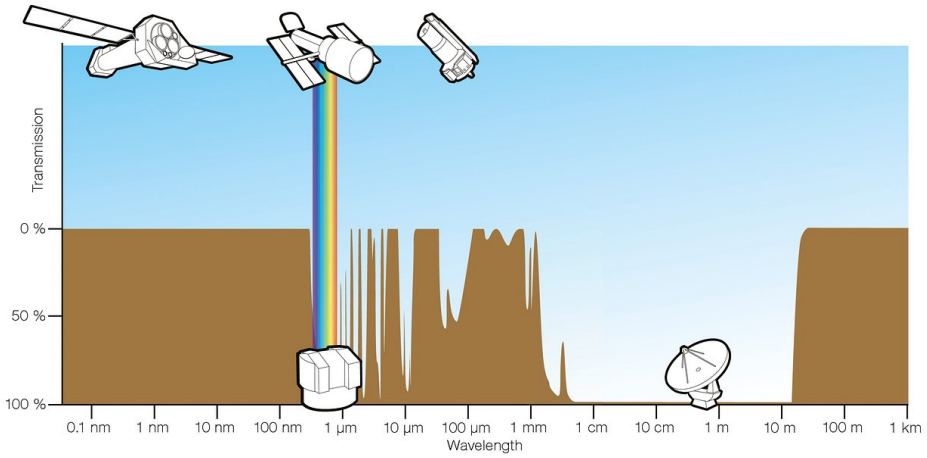

FIGURE 1.6: The brown curve shows atmospheric transparency at a given radiation wavelength from space. Ground-based astronomy has atmospheric windows to which it is confined, namely the visible (indicated by the rainbow) and radio (1 mm to 10 m) windows. Observations can be done outside the atmospheric windows using space telescopes such as XMM-Newton, Hubble and the Spitzer Space Telescope. Image credit: ESA/Hubble (F. Granato). Condon and Ransom (2016)

1.3 Neutral hydrogen as a probe of galaxy evolution

The most common element in the universe is hydrogen, which has been observed from large cosmological scales to the small pc-scales at the centre of galaxies. Neutral atomic hydrogen, H I , is important for understanding how various physical processes govern galaxy formation and evolution because it is a required transitory stage for star formation. Neutral hydrogen first needs to cool and transform into a molecular phase before it can fuel star formation as stars in the form of H_2.

The current radio telescopes are able to measure the H I 21 cm emission at $z \lesssim 0.25$ for direct detections of H I emission in galaxies, providing a direct H I mass estimate. This emission emerges from the hyper-fine splitting of neutral hydrogen from the ground state into two levels due to the electron and proton spin-spin interaction. A photon of rest wavelength, $\lambda \approx 21$ cm (frequency, $v \approx 1420$ MHz), is emitted when an electron in the upper energy level decays into the lower energy state (Péroux and Howk, 2020).

Atomic and molecular gas distributions are related to star formation morphologies. Their gas morphologies can be highly organised, defined patterns and not necessarily randomly-distributed clouds of interstellar material (ISM). The 21 cm emission line of atomic hydrogen is, in general, optically thin and not affected by extinction. Because HI typically has a larger extent than the optical/infrared components, it can serve as a much longer timescale tracer of external and influences on the galaxy's dynamics (Broeils and Rhee, 1997). This is advantageous as the total H I mass can be directly derived from the surface brightness maps. These H I maps also provide information regarding the kinematics and dynamics of the ISM as well the distribution and existence of dark matter in a galaxy (Buta, 2011).

There are three morphological points that H I maps reveal: (1) star-forming features, spiral arms, rings and pseudorings have enhanced surface brightness (Buta,

2011); (2) the H I gaseous disk extends past the optical extent (Buta, 2011); (3) wind-blown holes driven by supernova and star formation (Buta, 2011).

Morganti and Oosterloo (2018), discuss how the H I emission line improves of understanding of galaxies' kinematics, structure and evolution. Namely, H I emission played the key role in discovering dark matter properties in galaxies and showing the importance of gas accretion and circulation in the evolution of galaxies and the interaction of galaxies with their environment. Hence, H I is one of the main scientific drivers for the Square Kilometre Array (SKA) construction and its pathfinder and precursors, such as MeerKAT (Morganti and Oosterloo, 2018).

H I can also be observed in absorption. This absorption line is produced because of H I in front of a bright radio continuum source whose photons are absorbed at the rest frame 21 cm line. H I absorption is very useful as we are able to investigate processes and conditions in the ISM at large and small spatial scales, as well as in objects at much higher redshifts than what is possible with H I emission line. Associated absorption work is the H I absorption setting where the H I absorbing gas is part of the extragalactic object that produces the background radio continuum, for example, an AGN, as well as the active relationship between the gas and the continuum source (Morganti and Oosterloo, 2018).

Absorption studies focus on AGN and their interaction with the ISM of the same object because the absorbing gas and the bright continuum source are located in the same galaxy. One of the primary reasons for this study is to observe the general ISM structure and kinematics of galaxies with AGN and to study how it varies with different types of AGN. The shapes and widths of H I absorption lines can provide information on whether the ISM is in a rotating structure or are there indications of irregular gas distributions and therefore indirectly informing us of galaxy interactions. H I absorption studies also provides information as to what extent (large- or small-scale) gas structures of different kinds are found in different AGNs and hence informing us about the evolution's of these different objects (Morganti and Oosterloo, 2018).

H I absorption also gives us more insight on the gaseous regions surrounding the SMBH, the outflows and inflows of a system, to what extent is the gas in this region a fuel reservoir for the SMBH and whether it is the difference between active and quiescent SMBHs (Morganti and Oosterloo, 2018).

In contrast to H I emission, H I absorption observations are possible at much higher redshift due to the depth of the H I absorption line, in Jy, depending on the background continuum sources' strength. In principle, if a bright continuum source exists at high redshift, then H I absorption can be detected just as easily as at low redshifts. However, radio frequency interference (RFI) and receiver sensitivity limit the access to H I observations at high redshift. H I absorption can be imaged at high spatial resolution; for example, very long baseline interferometry (VLBI) reaches milli-arcseconds scales. These spatial resolutions are not in reach for H I emission due to column density sensitivity limits. For these reasons, H I absorption was preferred to study the H I evolution and properties of galaxies in the past. Now with technological developments and the construction of new telescopes, with improved sensitivity, H I emission studies are starting to develop more predominantly so we can get a comprehensive view of galaxies, their evolution and the role H I gas plays (Morganti and Oosterloo, 2018).

In the future, we can expect to use both H I emission and absorption as a probe of galaxy dynamics and structure for large samples of objects. In this thesis, we will profile one early example of this approach in NGC 6240.

1.3.1 Neutral hydrogen scaling relations in galaxies

We study galaxies in a group and large surveys to gain a better understanding of galaxies and their relations in comparision to one another. Parkash et al. (2018) select samples of galaxies to estimate relationships between H I gas mass, stellar mass and star formation rate. H I Parkes All-sky Survey catalogue (HICAT) and Wide-field Infrared Survey Explorer (WISE) galaxies are used in the samples where Galaxies from the H I Parkes All-sky Survey catalogue (HICAT) form the basis of the H I selected sample. Figure 1.7 shows the relationship between H I and stellar mass for the H I selected sample. From the graph, we can see that H I mass is a strong function of stellar mass with a Spearman's rank correlation, $r_s = 0,64$. The least-squares fit to the medians is,

$$log\ M_{H\,i} = 0.51(log\ M_\star - 10) + 9.71 \tag{1.1}$$

represented by the orange line in figure 1.7. Within 0.5 dex of the best fit relation is 68% of the H I masses.

Parkash et al. (2018) model the main sequence for galaxies using the spiral galaxies sample with stellar mass $\leq 10^{10.5}$ and get the main sequence to be

$$log\ SFR = 0.7(logM_\star - 10) - 0.09 \tag{1.2}$$

with a 1σ scatter corresponding to 0.27 dex (Parkash et al., 2018).

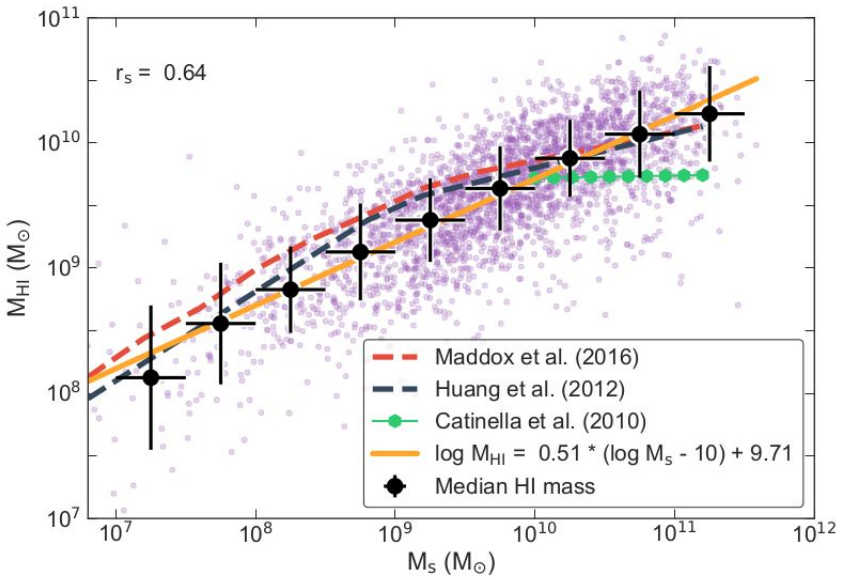

FIGURE 1.7: The relationship between H I mass and stellar mass for the H I selected sample. The orange line represents the least-squares fit to the median. This is compared to previous findings. Image credit: Parkash et al. (2018)

Wang et al. (2016) study a sample of 500 nearby galaxies covering a large range of H I mass (up to five orders of magnitude) to compare the H I size-mass (D_{HI}-M_{HI}) relation. They obtained the following relation:

$$log\ D_{HI} = (0.506 \pm 0.003)\, logM_{HI} - (3.293 \pm 0.009), \tag{1.3}$$

by performing a linear fit to the data points.

The H I mass function (HIMF) is another important relation for comparison between galaxies. The HIMF is the distribution of H I masses for the galaxies in the universe. From many surveys, it is found that the Schechter function (Schechter, 1976) fits the data well. The shape of the function follows a power-law exponent; the low mass slope on a logarithmic scale is $(\alpha + 1)$, then after the "knee" mass ($M_{\rm HI}$), the exponential declines (see figure 1.8). Jones et al. (2018) fit the HIMF to data from the ALFALFA (Arecibo Legacy Fast ALFA2) survey (Giovanelli et al., 2005) and is shown in figure 1.8. They find the Schechter function fit "knee" mass to be $\log(M_{\rm HI}h_{70}^2/{\rm M}_\odot) \approx 9.94$ which corresponds to the stellar mass of our own Galaxy, the Milky Way.

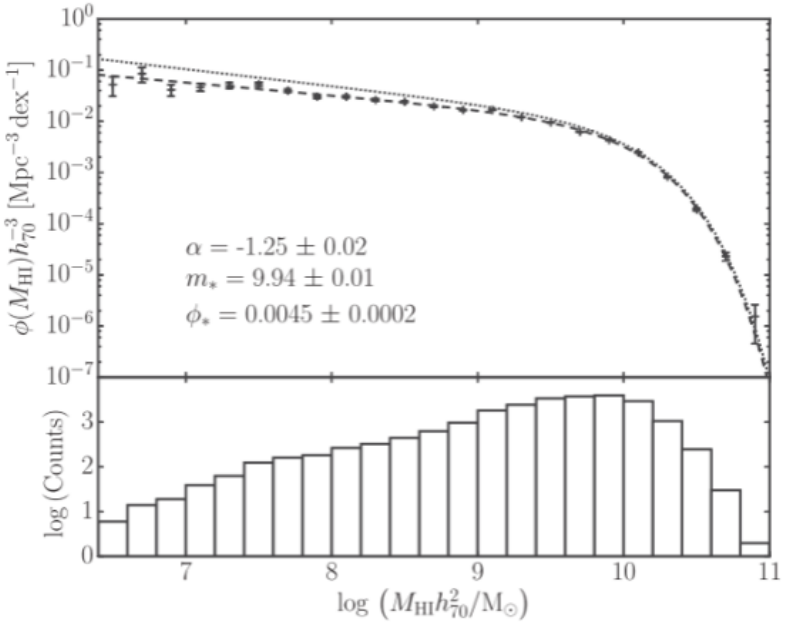

FIGURE 1.8: HI mass function for the ALFALFA survey. The top panel shows the H I number density, ϕ, as a function of the H I mass. The Schechter function parameters in the lower left corner correspond to the line of best fit for the data represented by the dashed line. The bottom panel is the number counts per logarithmic H I mass bin. Image credit:Jones et al. (2018)

These relations are important for the comparison of NGC 6240 with the general trend of normal star forming galaxies in the universe, discussed later in Chapter 4

1.4 NGC 6240

NGC 6240 is a very nearby ($z = 0.0245$) (Müller-Sánchez et al., 2018) ultra luminous infrared galaxy (ULIRG) with a reference position of RA (J2000) = 16h52m58.89s, DEC (J2000) = +02d24m03.3s (Hagiwara, Baan, and Klöckner, 2011). It is a key representative of its class and has been well studied at almost all wavelengths (Komossa et al., 2002).

ULIRGS are very luminous in the infrared. They are usually powered by super star bursts and/or hidden AGN. Many ULIRGS are interacting galaxies on the verge of forming elliptical galaxies. Studying local ULIRGS such as NGC 6240 is important to understand the physics of superwinds driven by nuclear starbursts, to search for hidden AGN and study the physics around galaxy formation (Komossa et al., 2002).

The dual nuclei of NGC 6240 has a separation of 750 kpc (1.6 arcsec) and is surrounded by a highly disrupted stellar disk structure along a position angle, PA = 25° east of North. The *K*-band luminosities for these two main emission peaks are $L(K) \sim 2 \times 10^9 L_\odot$ for the southern nucleus and $L(K) \sim 1 \times 10^9 L_\odot$ for the northern nucleus. These high luminosities correspond to large mass, $\geq 1 \times 10^9$ and $\geq 5 \times 10^8 M_\odot$ for the southern and northern nuclei, respectively (Tacconi et al., 1999). This suggests that the two nuclei are not simply starforming regions but rather individual galaxy nuclei hence NGC 6240 system is merging galaxies (Tacconi et al., 1999). This was later confirmed by Komossa et al. (2002).

Komossa et al. (2002) report the first high-resolution imaging spectroscopy of NGC 6240 in x-rays, performed by the *Chandra* x-ray observatory. This led to the discovery of two hard nuclei, coinciding with the optical infrared nuclei of NGC 6240. They report that both nuclei are active. The x-ray emission is also extended and highly structured, correlating closely with optical H α emission in NGC 6240, showing a relation to starburst-driven superwind activity. Figure 1.9 displays the spatial extent of x-ray emission. The hard x-ray observation is the best evidence for NGC 6240 containing AGN (Komossa et al., 2002).

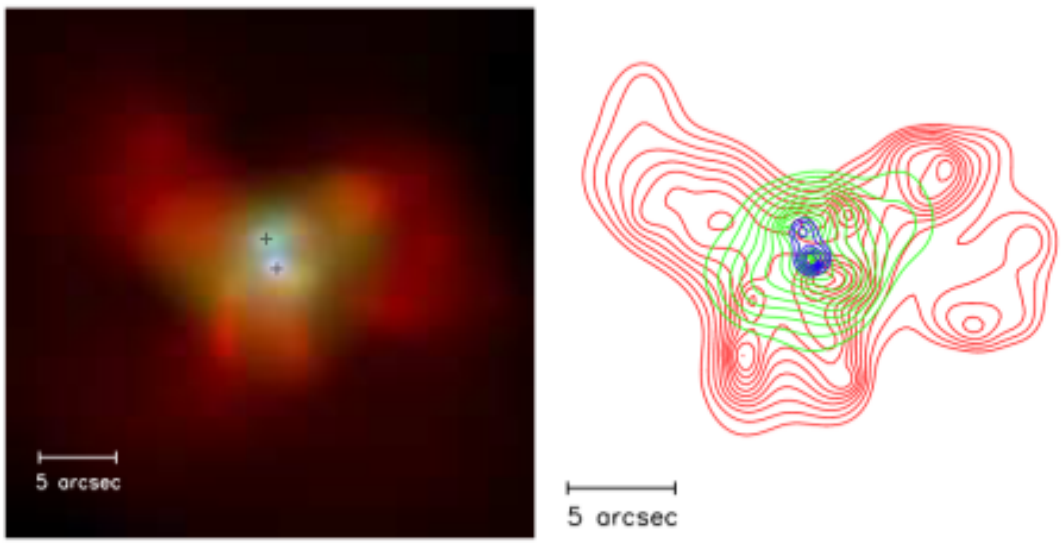

FIGURE 1.9: Multi-colour image (left) and contour plot (right) of x-ray emission in NGC 6240. Red is soft x-ray band (0.5-1.5 keV), green is medium x-ray band (1.5-5 keV) and blue is hard x-ray band (5-8 keV). 1" corresponds to 700 pc in this image. Image credit:Komossa et al. (2002)

Tacconi et al. (1999) presents on molecular gas in NGC 6240. They found that roughly half of the CO flux is concentrated between the nuclei in thick rotating disk structure, $\sim 500\ pc$. The disk is highly turbulent with velocity widths > 300 km s^{-1} FWHM. The mass of this central gas within the disk is $M_{gas} \sim 2 - 4 \times 10^9 M_\odot$ which accounts for a large fraction of the dynamical mass in this region, $M_{gas} \sim (0.3 - 0.7) M_{dyn}$. This is self-gravitating gas concentrations and may play a key role in the evolution of mergers (Tacconi et al., 1999).

Tacconi et al. (1999) performed CO 2 $\rightarrow$ 1 line observation of NGC 6240. Figure 1.10 shows this line spectra at 20 km s^{-1} resolution and a logarithmic image of integrated CO line emission. There you can see that in NGC 6240 majority of

the CO 2 $\rightarrow$ 1 emission is in the central 3 arcsec radius ($\sim 1.5kpc$). They detected 1220 Jy km s^{-1} of total CO flux. Figure 1.10 also displays the large velocity widths found almost everywhere within the central 3", showing the highly disturbed gas in NGC 6240. They expect that these large velocity widths are the cause of shocks and dissipation.

Tacconi et al. (1999) concludes that NGC 6240 is in an early merger stage when compared to other ULIRGs. The interstellar gas is settling between the nuclei and dissipating rapidly. The local random velocities will dissipate in only a few dynamical times, $< 10^7$ yr. After this happens, NGC 6240 will form a thin and dense central gas disk, which will be ready for major starburst. The luminosity of NGC 6240 will increase and the ISM will become more confined and hence resembling other ULIRGs more closely, such as Arp 220.

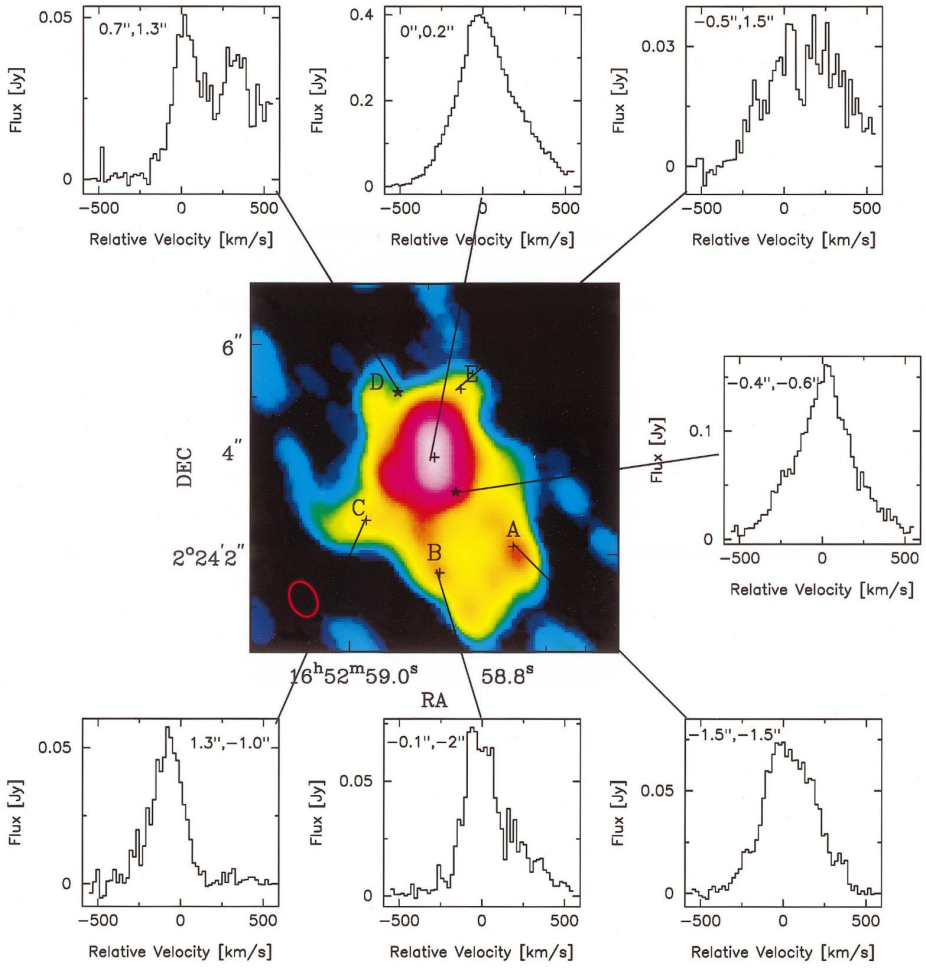

FIGURE 1.10: Figure from Tacconi et al. (1999) showing the superposed selected CO 2 $\rightarrow$ 1 line spectra and integrated flux distribution. The red ellipse in the lower left shows the synthesised beam with 0.5″ × 0.7″ FWHM resolution. The two asterisks show the two radio/infrared nuclei and the position of the spectra are marked with crosses.

In Müller-Sánchez et al. (2018) they report two spatially separated outflows in NGC 6240, namely black-hole-driven outflow of [O III]and starburst-driven outflow of $H\alpha$. The [O III]outflow is not spatially correlated with stellar continuum or molecular gas, which shows that it is not associated with tidal tails ftom the merger. This

black hole driven outflow has an outflow rate of 75 $M_{\odot}/yr$. The [O III] emission extends out to a distance of 3.7 kpc in the northeast direction with an opening angle $\theta_{out} \approx 50^{\circ}$. The [O III]cone is in the Seyfert region on the Baldwin-Philip-Terlevich (BPT) diagram due to its high [O III]/Hβ ratio. The [O III] cone is probably produced by the more powerful south-west nucleus. However, since the cone encompasses both nuclei, the contribution of the northern nucleus cannot be excluded, suggesting a combined narrow-line region from both AGNs (Müller-Sánchez et al., 2018).

The startburst-drive outflow, traced by $H\alpha$, has an outlfow rate of $10M_{\odot}/yr$ in the north-west direction and extends out to 90 kpc in loops, bubbles and filaments. This outflow is seen east and west of the nuclei and is not coincident with stellar continuum, see figure 1.11. From this, Müller-Sánchez et al. (2018) suggest that this outflow results from wind. $H\alpha$ outflow to the west could be from shock ionization from stellar winds. The northeastern nucleus is approximately three times fainter than the southwestern nucleus. The north eastern nucleus has a spectrum of a typical LINER (low-ionization nuclear-emission-line region) (Müller-Sánchez et al., 2018).

Figure 1.11 taken from Müller-Sánchez et al. (2018) presents a three-colour composite image of NGC 6240 centre (25"×25"), obtained by HSTs Wide Field Camera 3 (WFC). The green, red and blue colours on the image correspond to the continuum, $H\alpha$ and [O III]emission respectively. In this figure the two emission peaks can be seen clearly and are located at the position of the dual AGN. The continuum emissions are located mainly in the disk of the merger remnant, hence the extended continuum emission traces the stellar continuum. In region 3, there are knots and filaments of $H\alpha$ and [O III]supporting the scenario where both dual AGN and star-formation are contributors to the ionisation of extraplanar gas.

Müller-Sánchez et al. (2018) used HST and spectroscopic data from ground-based long-slit dual imaging spectrograph at APO/DIS. From UV and IR luminosity measurements, they found NGC 6240 has a high star formation rate SFR $> 100M_{\odot}/yr$. This, along with mass outflow rate, was used to evaluate the influence of negative feedback on the newly formed galaxy disk. The dual nuclei system is driving this negative feedback in NGC 6240. Müller-Sánchez et al. (2018) conclude that because the mass outflow of AGN and starformation is comparable to SFR, NGC 6240 is seen to be in a crucial phase in merger evolution of gas-rich galaxies. At this point, the star formation is starting to be suppressed. The only way to limit star formation activity and growth of newly formed post-merger galaxy, is the combined mass outflow.

Baan, Hagiwara, and Hofner (2007) report on H I and OH absorption observations made with VLA, A-configuration. They found strong concentrations of H I absorption towards the dual nucleus as well as weaker absorption across large areas of the extended radio continuum. Within the nuclear region, OH absorption was found. These observations confirm that between the nuclei, there is central gas accumulation. The turbulent dynamics of the system are confirmed by the large widths of H I absorption line across the central part of the source. Large-scale dynamics of the system, such as the foreground dust lane in the north west region, across radio structure, can be associated with some of the absorption components in NGC 6240. The origin of the symmetric superwind outflow has been identified as the southern nucleus and reveals that components from a nuclear starburst are blue shifted. Baan, Hagiwara, and Hofner (2007) used H I systemic velocities in a simple dynamical model, placing the galaxy associated with northern nucleus in front of the southern nucleus' galaxy. Therefore, between the two nuclei, the central disks of the galaxies would be superimposed. In this model, we'd expect the southern nucleus to have a larger absorbing column density than the northern nucleus, which is what Baan,

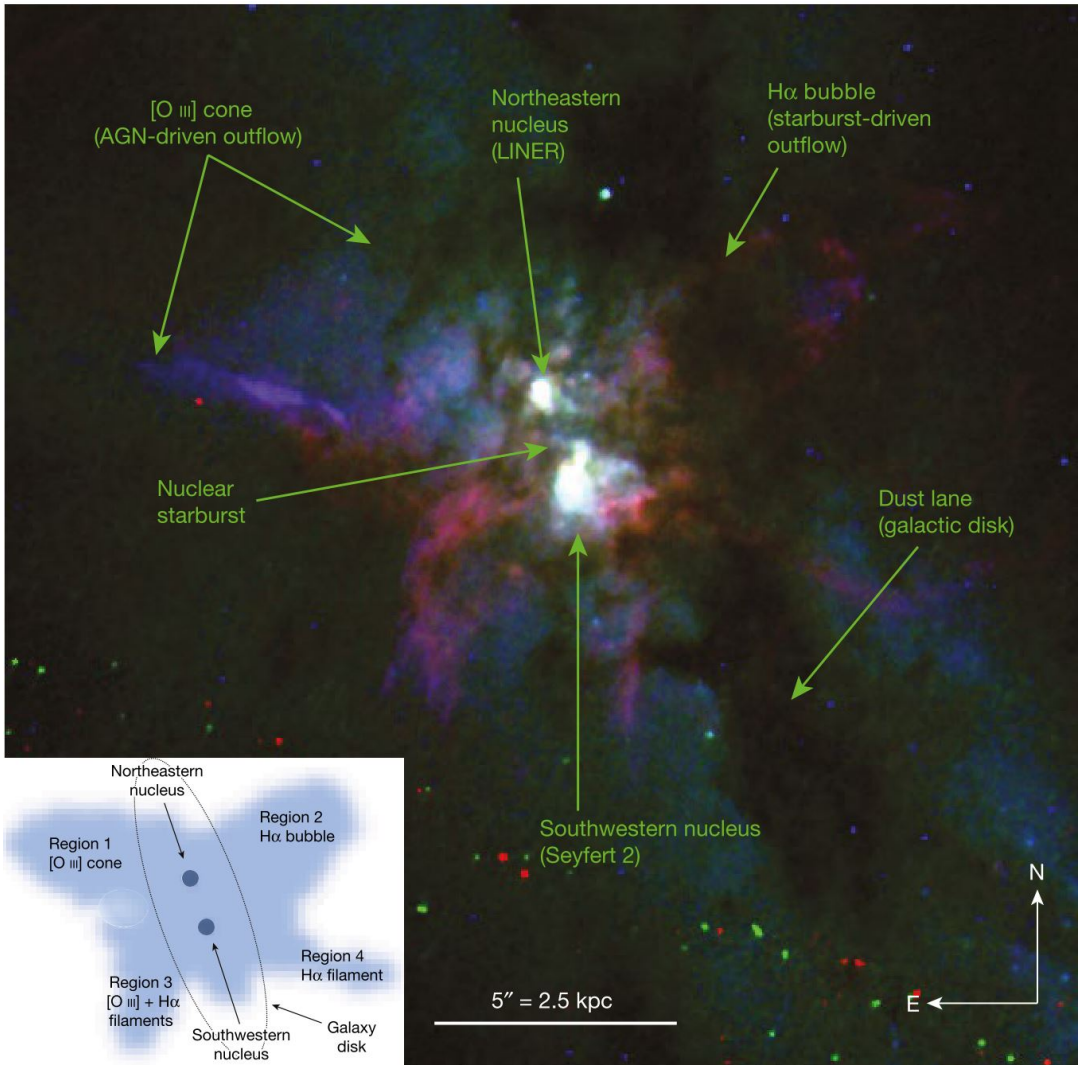

FIGURE 1.11: Figure from Müller-Sánchez et al. (2018) showing the three colour composite image of NGC 6240 obtained by HST of $H\alpha$, [O III]and V-band continuum emission in red, blue and green respectively. The central 25″ × 25″ is labelled, identifying the main structures. HST narrow-band filters are used to identify morphological structures in the butterfly-shaped region of NGC 6240 is shown in the inset.

Hagiwara, and Hofner (2007) found. The southern nucleus had a column density 1.26 times larger than the northern nucleus (Baan, Hagiwara, and Hofner, 2007).

Figure 1.12 taken from Baan, Hagiwara, and Hofner (2007) gives the H I absorption spectra of NGC 6240 in the extended emission region. N1 represents the southern nucleus and N2 the northern nucleus. The H I absorption profiles of these nuclei have similar spectra with full width at zero intensity, approximately 900 km s^{-1}. However, there are some note worthy differences; the absorption at N2 is 1.7 times stronger and more symmetric than at N1, which is skewed. From figure 1.12 we can see that the absorption columns vary greatly and are seen over a velocity range of $\sim$ 900 km s^{-1}. The three reason as to what causes these velocities is the rotation in each galaxy, the two galaxies' orbital velocity component and the interaction causing inflow and outflow.

OH absorption at 1667 and 1665 MHz, reported by Baan, Hagiwara, and Hofner (2007), was only found in nuclear region extending 1.25 $\times$ 1.0 kpc. The 1667 MHz line width is largest between the two nuclei, similar to the H I absorption. However, the OH line width, 80 km s^{-1}, is noticeably smaller than that found in H I , 150 km s^{-1}(Baan, Hagiwara, and Hofner, 2007). The OH line widths become narrow in the region where the velocity field is confused and goes down to a very low 20 km s^{-1}further west. The column density of the OH absorption is largest between the nuclei and north of the south nucleus. 60 % of the central gas structure is the column densities at the two nuclei. Therefore OH is less affected by merger dynamics when compared to H I as seen by the significantly smaller velocity widths of OH (Baan, Hagiwara, and Hofner, 2007).

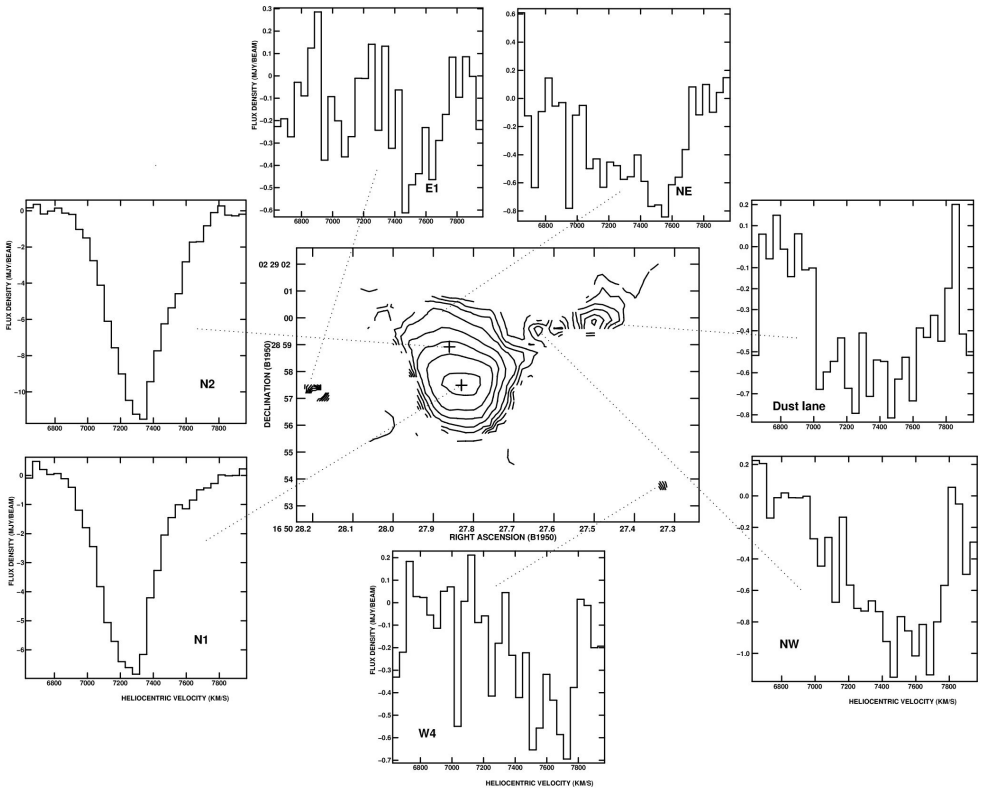

FIGURE 1.12: H I absorption spectral signatures in NGC 6240 taken from Baan, Hagiwara, and Hofner (2007). In the centre is the moment zero map of integrated H I absorption surrounded by the spectra at seven locations with velocity tick marks of 6800-7800 km s^{-1}.

H I emission in NGC 6240 has not yet been detected, but MeerKAT is well placed to do so hence motivation to observe this source. From studying the ionized and molecular gas in the system we expect H I emission to be disrupted and surrounding the centre of NGC 6240. This thesis will look at both H I emission and absorption, the distribution of H I gas and its kinematics. The H I absorption observation limits our view to high column density H I in front of the continuum sources. These results will be compared to previous findings to improve our understanding of this rich merger system.

1.5 Thesis outline

Neutral Hydrogen, H I , is a key ingredient in studying galaxy formation and evolution. With current telescopes, which have improved sensitivity, such as MeerKAT, we are able to detect the 21 cm H I emission line. We want to study H I emission and absorption in merger systems such as NGC 6240 to understand the role H I plays in galaxy formation and evolution and use this information to identify these systems at higher redshifts. NGC 6240 is the perfect candidate to study this as it is a prototypical galaxy merger, nearby ($z = 0.0245$) and dual AGN.

This thesis layout is as follows: An introduction to radio interferometry, the MeerKAT Telescope and interferometric calibration and imaging are presented in Chapter 2. Chapter 3 presents the MeerKAT observations of NGC 6240. Here we see that H I emission lies in two planes, one in line with the primary galactic disk and the other in line with a neighbouring galaxy, south-east plane. The orientation of the H I absorption is also in line with the galactic disk. The H I properties are also presented in chapter 3.

Chapter 4 discusses these results, completing the picture of H I in NGC 6240, reconciling H I absorption and emission. We also discuss the evidence for interaction between NGC 6240 and the neighbouring H I galaxy. Chapter 5 presents the conclusions of this project and discusses future work.

Throughout this thesis we assume Hubble constant value of $H = 70\,\mathrm{km\,s^{-1}\,Mpc^{-1}}$, the redshift of NGC 6240 to be $z = 0.0245$ with corresponding recession velocity, $V_\mathrm{r} = 7339\ \mathrm{km\,s^{-1}}$.

Chapter 2

Observations, calibration and imaging

2.1 Radio interferometry

Radio astronomy began with single dish telescopes starting with Karl Jansky in 1933 (Jansky, 1957), who discovered radio emission of a non-terrestrial nature. The angular resolution, θ, of a single telescope is dependent on the diameter of the dish, $\theta \approx \lambda / D$, where λ is the observing wavelength and D the diameter of the dish. The larger the diameter, the higher the angular resolution for a given observing wavelength. However, due to engineering and cost constraints, we are limited in the size of these single dish telescopes (Thompson, Moran, and Swenson, 2017). For example, the largest single dish radio telescope is the FAST telescope in China with a diameter of about 500 m (Jiang et al., 2019).

In the early era of radio astronomy, it quickly became clear how important it was to accurately measure the positions of radio sources in order to correctly associate them with optical sources with known redshifts, enabling intrinsic properties to be derived (Thompson, Moran, and Swenson, 2017). This requirement and the need to classify them morphologically led to radio interferometers and their dramatic enhancements that enabled higher fidelity imaging. Martin Ryle and his group in Cambridge developed the first radio interferometer in 1946. This and the technical breakthrough of Earth-rotation aperture synthesis led to Martin Ryle sharing a Nobel Prize for Physics in 1974, alongside Antony Hewish for the co-discovery of the pulsar. Rather than a single dish, radio interferometers are an array of radio antennas. The voltages of each antenna are cross-correlated to synthesize a single telescope. The distance between two antennas, known as a baseline, can be as long as 10,000 km (if fixed to the earth, longer if a spacecraft is used), drastically improving the angular resolution we are able to achieve. The angular resolution of an object or field observed by a radio interferometer is given by,

$$\theta \approx \frac{\lambda}{B}, \tag{2.1}$$

where θ is angular resolution in radians, B is the maximum baseline length (in contrast to the diameter of a single dish), and λ is the observing wavelength (Thompson, Moran, and Swenson, 2017).

An incoming wavefront will arrive at each antenna at a different time, except in the special case that the source is exactly at an hour angle of zero. These geometric delays are corrected prior to the cross-correlation of each pair of antenna voltage streams. This is illustrated in figure 2.1 which demonstrates the geometric time delay, τ_g, and the instrumental time delay, τ_i. The delay corrections applied prior to

the correlation process include station location models, source position, earth rotation, atmosphere and tidal loading, amongst others. Despite the complexity and care taken, residual delays will remain, but these can largely be corrected for in the post-correlation calibration process.

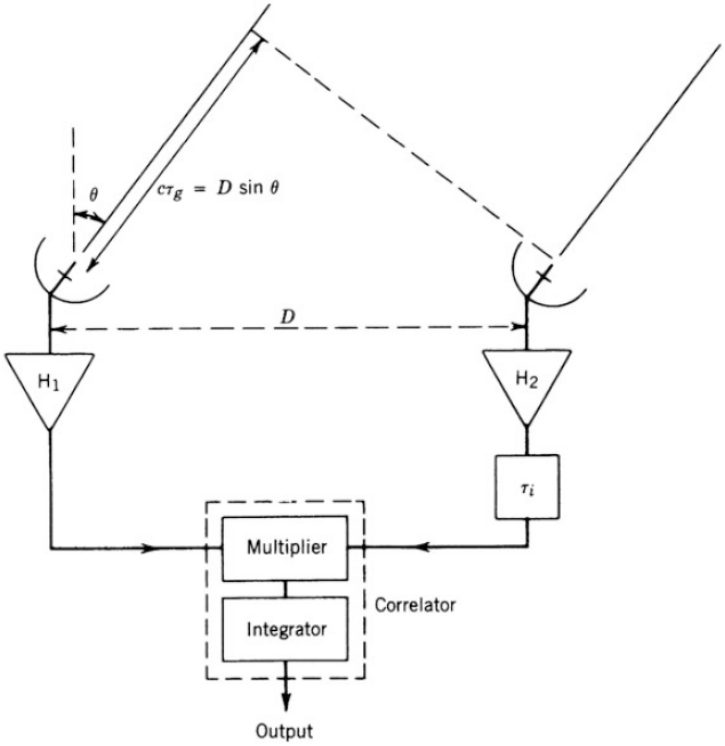

FIGURE 2.1: A simple dual antenna interferometer showing the geometric time delay, τ_g, instrumental time delay, τ_i, H_1 and H_2 bandpass amplifiers and the correlator, which consists of a multiplier and integrator. Image credit: Thompson, Moran, and Swenson (2017)

An interferometer measures visibilities, V_{ij}, between antenna i and antenna j, which are samples of the 2D Fourier transform of the sky brightness distribution. The Fourier transform is a mathematical operator that decomposes signals into sinusoidal components. Visibilities are complex numbers and can be written in the form of amplitude, A, and phase, θ.

$$V_{ij}(u,v) = A\, e^{i\theta} \tag{2.2}$$

Amplitude encodes the intensity of flux observed and the phase encodes the location of the flux measured (Middelberg and Bach, 2008).

The antenna co-ordinates are projected onto a plane known as the (u,v) plane, which is perpendicular to the projected vector that connects the interferometer elements, baselines, towards the astronomical source. The co-ordinates of the plane are u and v, most often measured in wavelengths. Each interferometric visibility has (u,v) co-ordinates represented by a vector from the origin of the plane, which describes the antennas separation distance and orientation (e.g. Thompson, Moran, and Swenson, 2017; Middelberg and Bach, 2008).

The visibility function, V_v, given by equation 2.3 is the input observers use for further processing,

$$V_v(u,v) = \int\int \mathrm{A}_v(l,m) * \mathrm{I}_v(l,m) * e^{-2\pi i(ul+vm)} dldm. \tag{2.3}$$

The co-ordinates (l, m) are directional cosines, where the (l, m)-plane is known as the image plane. The sky intensity distribution is given by I_v. The function A_v, is the antenna response or primary beam function and is included in the visibility function to account for the interferometer sensitivity (e.g. Middelberg and Bach, 2008).

Not all Fourier components are sampled by an interferometer due to the limited number of antennas and baseline length range. Interferometers typically measure arcs in the (u, v) plane rather than points. This is due to the rotation of the earth, which changes the projected baseline length and orientation, known as earth rotation synthesis. This is beneficial; as the observation progresses, a wider range of spatial frequencies of the source are sampled. A pair of conjugate arcs and their distance from the origin of the (u, v) plane represents one baseline and its length. Therefore increasing the number of antennas increases the number of baselines and hence visibilties. This improves the (u, v) coverage leading to better constraints on sky brightness distribution and hence improved image fidelity (Middelberg and Bach, 2008).

Since only a finite number of points of the (u, v)-plane are sampled, the inverse Fourier-transform will create an imperfect image, known as the dirty image. The dirty image is the convolution of the true sky brightness distribution with the interferometer's point spread function (PSF) (Thompson, Moran, and Swenson, 2017). In aperture synthesis, the PSF is the Fourier transform of the coverage in the (u, v)-plane (Middelberg and Bach, 2008). An example of (u, v)-coverage and its corresponding point-spread function is given in figure 2.2 for a 7.2 hour observation of NGC 6240 with the MeerKAT telescope.

2.2 MeerKAT telescope

MeerKAT is a South African radio interferometer located in the northern Karoo desert and is a precursor to the Square Kilometre Array (SKA) mid-frequency telescope. MeerKAT comprises of 64 offset Gregorian parabolic dish antennas, 13.5 m in diameter (Jonas and Team, 2016). These dishes consist of a primary reflector and subreflector, feed horns, digitizers and cryogenically cooled receivers which are mounted on a feed indexer. These, along with support structures and drive systems, are all mounted on a pedestal. This dish design allows the positioning of four receiver systems near the subreflector without obstructing the clear optical path (Camilo et al., 2018).

Currently, there are only two receivers covering a frequency range of 580 MHz to 1670 MHz in two bands that overlap, namely the UHF-band ranging from 580 MHz - 1015 MHz and the L-band ranging from 900 MHz - 1670 MHz. The Max Planck Institute for Radio Astronomy (MPIfR) will be providing S-band receivers which will cover a frequency range of 1750 MHz - 3500 MHz (Jonas and Team, 2016).

The inner core with a 1 km diameter has 48 out of the 64 antennas, including the shortest baseline of 29 m. The remaining 16 antennas are spread beyond the core up to a maximum baseline of 8 km, see figure 2.3 (Jonas and Team, 2016). Therefore at a central frequency of 1283 MHz, MeerKAT is able to recover a wide range of angular scales, 5" to 27′. A summary of MeerKAT's main characteristics is given in table 2.1

[1] //skaafrica.atlassian.net/servicedesk/customer/portal/1/topic/bc9d6ad2-8321-4e13-a97a-d19d6d019a1c/article/277315585

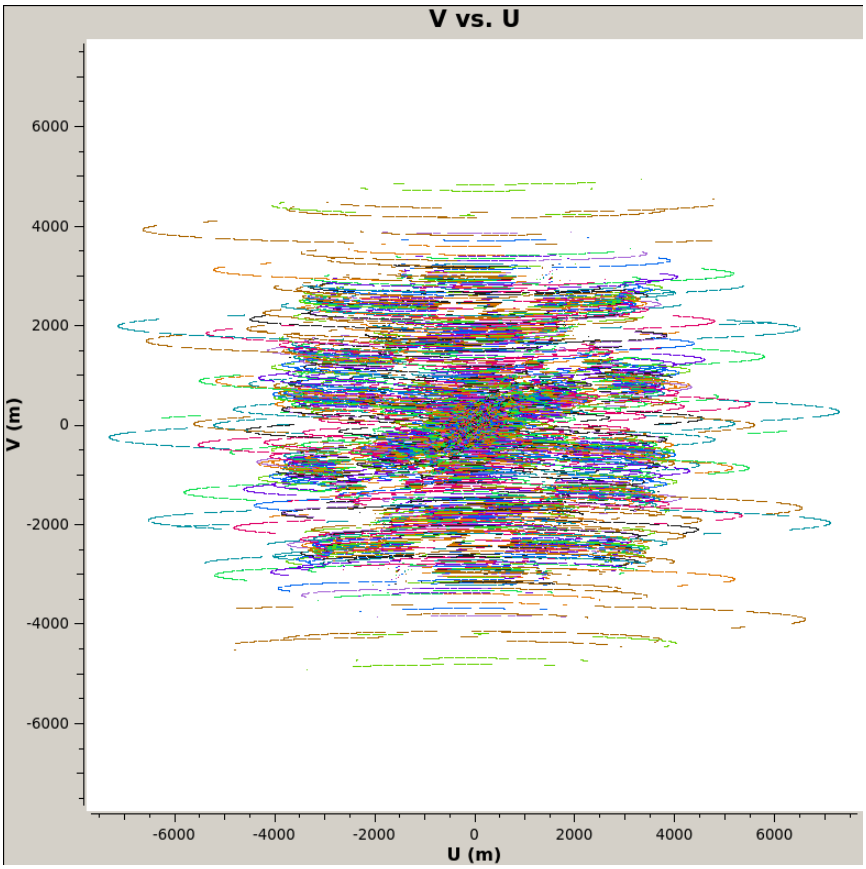

FIGURE 2.2: The (u, v) coverage for the 7.2-hour NGC 6240 MeerKAT observation for a single narrow frequency channel centred on 1385 MHz. Each baseline is represented by a different colour arc. The (u, v) co-ordinates are in meters.

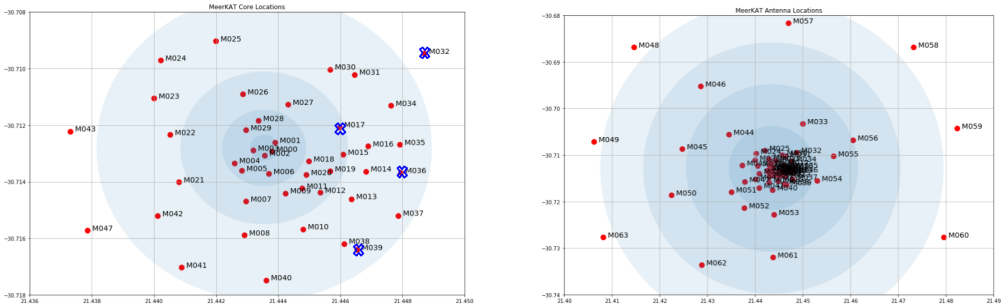

(A) Antenna locations in the core

(B) Antenna locations in the extended region.

FIGURE 2.3: Positions of the MeerKAT antennas in the core and the extended view. The blue crosses represent the antennas that were not available during this observation. Image from SARAO documentation[1].

MeerKAT has ten large-scale survey projects with science goals related to those of the SKA as it is a precursor to the SKA mid-frequency array (SKA1-mid). These projects will use approximately 68% of MeerKAT's full-scale operations for the first five years. Five of these projects involve atomic hydrogen, H I , and are described briefly below (Jonas and Team, 2016).

MeerKAT Telescope	
Location	Karoo, South Africa
No. of antennas	64
Dish diameter	13.5 m
Shortest baseline	29 m
Longest baseline	8 km
Angular scale range	5"- 27′
L-band frequency range	580-1670 MHz

TABLE 2.1: A summary of the main characteristics of the South African MeerKAT telescope.

1. LADUMA: This is an ultra-deep H I emission survey that goes out to a redshift of 1.4. The goal is to investigate cosmic evolution over the last 9 Gyr of H I galaxies. Both the UHF and L-band receivers are being used in order to cover the redshift range for a single pointing (Blyth et al., 2016). Recent publication by Glowacki et al. (2022).

2. MHONGOOSE: This survey uses a sample of 30 galaxies located within 30 Mpc that have a large H I mass range varying by five orders of magnitude. The neutral hydrogen distribution and dynamics of these galaxies are surveyed. With MeerKAT's unique capabilities, we are able to detect and map with detail faint gas from the surroundings that are falling into galaxies (De Blok et al., 2017). Recent publication by Maccagni (2022).

3. Fornax: A deep H I emission line survey studying the dynamics of H I in the Fornax cluster and connecting this to the cosmic web. Fornax is the largest cluster in the southern hemisphere and is nearby (20 Mpc). These observations are expected to yield $\sim$ 100 H I detections. The spatial resolution will reach $\sim$ 1 kpc for gas dynamics and $\sim$ 10 kpc of resolution for the cosmic web (Kleiner et al., 2021). Recent publication by Loni (2022).

4. MALS: This is a survey of H I and OH absorbers. For galaxies at a redshift ranging from 0 to 2, it will map the evolution of cold atomic and molecular gas. It is probing the evolution of star-formation rate density ($z \approx 2$) to the current universe with low-level observations (Gupta et al., 2017). Recent publication by Maina et al. (2022).

5. MIGHTEE: The MeerKAT International GHz Tiered Extragalactic Exploration (MIGHTEE) Survey (Jarvis et al., 2017) is a Large Survey Project (LSP) conducted over four of the most well-studied extragalactic deep fields, namely COSMOS, XMM-LSS, ECDFS and ELAIS-S1. These total to 20 deg^2 with μJy sensitivity at GHz frequencies allowing a plethora of radio continuum extragalactic science, as well as the detection of HI in a significant number of galaxies at $z = 0.2$ and rare H I -massive galaxies up to $z \sim 0.5$. Recent publication by Sinigaglia et al. (2022).

2.3 MeerKAT observations of NGC 6240

MeerKAT L-band observations were carried out on NGC 6240 on 1 July 2019 for a total on-source time of 7.2 hours. The 4K correlator mode was used for the observations, 4096 channels with a frequency resolution of 209 kHz, corresponding to

TABLE 2.2: MeerKAT observations of NGC 6240

Observing Date	2019-06-01
Unavailable antenna	m017, m032, m036, m039
Duration (hr)	8.0
On-source (hr)	7.2
Reference frequency (MHz)	1386.5
No. Channels	701
Frequency resolution (kHz)	209

TABLE 2.3: Imaging parameters

Pixel size	1.3 arcsec
Restoring beam FWHM	12×8 arcsec^2 P.A. = -26 deg
N_{HI} sensitivity (1σ)	$\sim 2 \times 10^{20}$

44 km s^{-1} at $z = 0$, and a time resolution of 8 seconds. For post-processing, the data was split into 701 channels at the full 209 kHz frequency resolution, for a frequency range covering approximately 1300-1440 MHz. 60 out of the 64 MeerKAT antennas were used. The unavailable antennas were; m017, m032, m036 and m039 (see figure 2.3).

The position of NGC 6240 and hence the MeerKAT pointing for this observation is RA=16h52m59s and DEC=+02d24m04s. PKS 1934-63 was used as the absolute flux and bandpass calibrator. To monitor and solve for time-varying complex gains, we interleaved observations of NGC 6240 with the calibrator source, J1550+0527. Table 2.2 shows a summary of the observations.

2.4 Calibration and imaging

The data were reduced using OXKAT[2] , a semi-automated MeerKAT data analysis pipeline. OXKAT was developed specifically for MeerKAT continuum data reduction making use of several publicly available radio interferometry software to carry flagging, calibration, and imaging steps (Heywood, 2020). It utilises a suite of packages, including CASA[3] (McMullin et al., 2007), WSCLEAN[4] and the TRICOLOUR[5] flagging software. The ilifu Cloud facility[6] was used for all data reduction, imaging and analysis, run within SINGULARITY containers.

The top-level calibration strategy starts with so-called first Generation Calibration (1GC), which consists of flagging, absolute flux calibration, and correction of atmospheric and instrumental effects on the data using well-characterised calibration sources. The next stage is a series of iterative steps, sometimes referred to as Second Generation Calibration (2GC), which includes self-calibration and the utilisation of imaging and deconvolution algorithms, such as WSCLEAN. Once this is complete, continuum subtraction is performed to isolate the spectral line data. In the

[2]https://github.com/IanHeywood/oxkat
[3]https://casa.nrao.edu/
[4]https://gitlab.com/aroffringa/wsclean/
[5]https://github.com/ska-sa/tricolour
[6]https://www.ilifu.ac.za/

below sections, we describe the key steps in the 1GC and 2GC workflows, as applied in the MeerKAT NGC 6240 data processing.

2.4.1 First generation calibration (1GC)

First generation calibration is also known as cross-calibration. Several of the cross-calibration tasks used in the OXKAT pipeline are from the CASA suite. Cross-calibration is necessary to correct instrument imperfections and the effects of the environment, atmosphere, system faults and inaccuracies.

Known radio frequency interference (RFI) channels, as well as unknown RFI sources, are removed from the data. The autoflagger package, TRICOLOUR, was used to flag out other intermittent, lower level RFI (Heywood, 2020).

The instrumental and atmospheric gains change throughout the observation time. These changes are estimated through the calibrator observations as they have a simple model and slowly varying source structure. This makes it possible for the calibrator gain solutions to be solved and transferred to the target field, effectively compensating for some of the errors in the visibilities and allowing the measurements to be tied to a physical flux scale (Thompson, Moran, and Swenson, 2017).

Table 2.4 summarises four of the essential calibration steps and the type of calibrator each requires. The same calibrator source can, in principle, be used for two or more as they all need a very bright point-like or well-modelled source. For these observations, PKS 1934-63 was the bandpass and absolute flux calibrator.

For time variable complex gain calibration, a unique calibrator is chosen close ($\lesssim 10\,\mathrm{deg}$) to the target source. The brightness does not need to be as high as for the absolute flux and bandpass for this calibration. Ideally, the calibrator should be a compact like source to solve for the time-varying complex gains throughout the observation. J1550+0527 is the gain calibrator for these observations.

2.4.2 Imaging

The process of imaging includes the Fourier transformation of visibility data that are interpolated onto a uv-grid. This is followed by the application of the `CLEAN` algorithm (or alternative), which is a non-linear deconvolution algorithm. The (multi-scale) `CLEAN` deconvolution process can improve the limited spatial frequency coverage by allowing visibilities that were not measured to take on nonzero values within some general image constraints (Thompson, Moran, and Swenson, 2017).

Högbom (1974) developed one of the most widely applied numerical deconvolution processes in `CLEAN`, mostly applied in the image domain (l, m). It is an essential procedure for creating higher fidelity, higher-dynamic range images from incomplete (u, v) data sets. `CLEAN` was initially developed on the assumption that the sky can be reasonably modelled by a collection of point sources (Thompson, Moran, and Swenson, 2017). However, as interferometers have improved, this has increasingly proved to be a limiting assumption for more complex sources.

There are five fundamental steps to the `CLEAN` algorithm:

1. Use a Fourier transformation of the visibility and spatial sensitivity function to compute the image and the response to a point source. These functions are commonly referred to as the synthesised intensity, "dirty image", and the synthesised beam, "dirty beam", respectively. In the (l, m) plane, the sample point spacing (i.e. pixel size) should be at most one-third of the synthesised beam width (Thompson, Moran, and Swenson, 2017).

Calibration	Description	Calibrator type
Absolute flux	Sets the flux scale to convert measurement units to physical units.	- Very Bright ($\gtrsim$ 10 Jy) - invariant - typically unresolved and/or well-modelled structure
Bandpass	Calibration of instrumental bandpass corrects for the imperfect frequency response of the instrument. Only one or two bandpass calibrations typically need to be performed per observation of approximately 8 hours as the relative gains of different channels don't vary significantly with time.	- Very Bright ($\gtrsim$ 10 Jy) - invariant - Typically unresolved and well-modelled structure and spectrum - position need not be close to target.
Delay	Removes phase delay errors caused by atmospheric delay along the line of sight of each antenna, instrumental delays and correlator model imperfections.	Can use all the calibration sources as well as target source for this calibration, if there is enough flux.
Gain	This calibration step is interleaved with a duty cycle of order $\sim$ 10-20 min, to determine complex valued gains by tracking the evolution of the local effects. For example the atmosphere and the elastic deformation of the antenna structure due to gravity.	- Must be close to target ($\lesssim$ 10 deg) - relatively bright ($\gtrsim$ 100 mJy)

TABLE 2.4: Summary of four of the most important calibrations and desirable calibrator source properties

2. In the image, locate the highest intensity point and subtract an amplitude-scaled dirty beam (point source response) centred on that position, including the side lobe pattern. The factor by which the peak amplitude of the subtracted dirty beam differs from the corresponding image amplitude is given by γ, also known as the loop gain. γ is typically set to a value of ~ 0.1. The position and amplitude of the removed component are recorded by creating a model by inserting the delta-function component, creating the cleaned image (Thompson, Moran, and Swenson, 2017).

3. Repeat step 2 iteratively until all the significant source structure from the image has been removed. An indication of this condition, for example, arises when after a clean-component subtraction, the rms level of the residual intensity does not decrease or when one starts to notice the removal of a large amount of negative components. At this point, the residual intensity distribution mainly consists of noise and calibration artefacts (Thompson, Moran, and Swenson, 2017).

4. Each delta function in the cleaned model is convolved with a clean-beam function. A Gaussian, or a similar non-negative function, is usually chosen as the

clean (or restoring) beam. The FWHM of the Gaussian is equal to that of the original synthesised (dirty) beam. This prevents over-interpretation and hence `CLEAN` performs an interpolation of the (ν, v) plane (Thompson, Moran, and Swenson, 2017).

5. The residual intensity from step 3 is added to the clean-beam image. This is the final output of the process (Thompson, Moran, and Swenson, 2017).

In the imaging process, we apply certain weighting schemes. One type of weighting is natural weighting, where the same weight is applied to all measurements regardless of (u, v)-distance to obtain maximum signal-to-noise ratio, usually applied for data obtained with a uniform array of antennas and receivers. However, natural weighting for many arrays could result in poor beam shape and angular resolution due to over-represented shorter spacings in a compact core (Thompson, Moran, and Swenson, 2017). Uniform weighting is another type of weighting scheme at the other end of the spectrum, where the beam shape has lower sidelobes resulting in higher angular resolution but poorer sensitivity (Thompson, Moran, and Swenson, 2017).

In practice, natural weighting is the best weak point source detection strategy. In contrast, uniform weighting will produce an image with higher angular resolution and lower sidelobes. To ease the trade off between the two weighting schemes, a continuous variation in weighting between the two was developed by a logarithmic parameterised scheme, known as Briggs weighting or ROBUST weighting. This weighting has a robustness factor, R, that ranges from -2 to 2 (in CASA definition) (McMullin et al., 2007). As R approaches $R = 2$ the weighting approaches natural weighting and as it approaches $R = -2$ it approaches uniform weighting. Therefore as the ROBUST parameter increases the angular resolution decreases but the sensitivity increases, revealing more diffuse emission (Thompson, Moran, and Swenson, 2017).

The data in this project is imaged and deconvolved using the software package WSCLEAN (Offringa et al., 2014). Three data cubes were created each with different BRIGGS weighting with ROBUST parameters of -1.2, 0.0 and 0.5 to address different scientific objectives.

2.4.3 Second generation calibration (2GC)

Self-calibration can improve the imaging dynamic range and fidelity. The NGC 6240 self-calibration process details are covered in greater detail in Magolego (2022, MSc thesis) and Magolego et al. (in prep.), who investigate the large-scale continuum properties of the same field. However, we briefly cover some of the key steps here before describing the spectral line imaging.

The self-calibration process starts by generating a post-1GC model image to create an initial sky-model of the target field, using a shallow unmasked clean down to 50μJy beam^{-1} and `robust` weighting of -0.3. A mask is generated from this image using a local rms threshold of 10σ due to the artefacts present in the 1GC image, many of which are associated with the bright and extended continuum emission associated with NGC 6240. The imaging is repeated with the same parameters with this mask in place, generating the first model, which is then Fourier-transformed into the `MODEL` column of the measurement set.

The initial or improved sky-model is then used to refine solutions of complex gains in three separate rounds. The first round refines the delay calibration on a per-scan ($\sim$1 min) interval, using the CUBICAL solver. The second and third rounds used the standard CASA `gaincal` task on 8-sec time intervals (given the large amount of

flux in the field), solving for phase-only and amplitude and phase complex gains, respectively. In each round, the improved solutions are applied to the visibilities and imaged once again to iteratively improve the sky model to achieve a continuum rms of $\sigma \sim 6\mu$Jy beam^{-1}.

2.4.4 Spectral line imaging

In spectral line imaging, we produce a distribution of pixels in three dimensions, (l, m, v), called a data cube. The data cube contains images for each frequency channel, the width of which is specified by the user. In order to interpret the data cube in a physical way, the frequency dimensions, v, Doppler shift is converted to radial velocity, v_r. This is done with respect to the spectral line rest frequency.

The calibrated data contains both continuum and spectral line data. Continuum subtraction is performed in both the (u, v)-plane and image domain to isolate H I line emission. The CASA tasks that are used to perform the continuum subtraction are UVSUB[7], in order to first subtract the clean model components from the corrected data. We then perform a first-order fit in the (u, v) domain using the task UVCONTSUB[8].

This leaves behind three continuum-subtracted datasets, which is then imaged at 209 kHz resolution to produce three H I spectral line cubes with ROBUST weightings of 0.5, 0.0 and -1.2. For each cube, we perform second-order image-plane continuum subtraction using the task IMCONTSUB[9].

Each cube was centred at the same position at the centre of the dual AGN in NGC 6240. The spatial and velocity extent of NGC 6240 is 54 kpc $\times$ 99 kpc $\times$ 833 km s^{-1}. The Point Spread Function full width at half maximum (PSF FWHM) ranges from 10×7 arcsec^2 to 22×12 arcsec^2 and position angle (P.A.) ranging from -26° to -24° for the three cubes. The exact values are given in table 3.1 for each cube.

2.5 Multi-wavelength data

To gain a more holistic understanding of the H I results and environment of NGC 6240, we use images and catalogues from observations at other wavelengths.

Data from the Hubble Space Telescope was used for wavelengths in the visible spectrum. The data was obtained using the Hubble Legacy Archive[10]. The observation was made with Hubble's wide field camera (WFC) and filter F435W, which corresponds to wavelengths from 3605.21 Å to 4881.63 Å.

Ultraviolet (UV) data was obtained from the Galaxy Evolution Explorer (GALEX)[11]. To trace the active star formation in NGC 6240 and its neighbours, we use near and far-ultraviolet images from the GALEX satellite (Morrissey et al., 2007). X-ray data was obtained from the *Chandra*[12] x-ray observatory to trace AGN activity.

[7] https://casa.nrao.edu/docs/taskref/uvsub-task.html
[8] https://casa.nrao.edu/docs/taskref/uvcontsub-task.html
[9] https://casa.nrao.edu/docs/taskref/imcontsub-task.html
[10] https://hla.stsci.edu/
[11] http://www.galex.caltech.edu/about/overview.html
[12] https://cxc.cfa.harvard.edu/csc/

Chapter 3

Results

This chapter will discuss the spectral line data products from neutral hydrogen MeerKAT observation of NGC 6240. We start with individual channel maps and then move on to representing these data cubes in a single image, namely the integrated intensity map and intensity-weighted velocity map for the H I emission. We then discuss the H I absorption analysis and finally the derived H I properties.

For all calculations the redshift of NGC 6240, $z = 0.02448$, was used from the CO (1-0) line shift given by Downes, Solomon, and Radford (1993). We use this value for redshift for ease of comparison since it is widely adopted in the extensive literature on the object.

3.1 Channel maps

Following the calibration, imaging and continuum subtraction steps described in chapter 2, a subcube was created to isolate NGC 6240, keeping the central 202 channels ranging from a recession velocity of 2 208 $\mathrm{km\,s^{-1}}$ to 11 481 $\mathrm{km\,s^{-1}}$. The difference between each channel, the channel width, is 46 $\mathrm{km\,s^{-1}}$ at $z = 0.02448$. The size of the subcube corresponds to 3.1 arcmin $\times$ 4.4 arcmin $\times$ 9273 $\mathrm{km\,s^{-1}}$.

The standard deviation per channel changes significantly due to different RFI occupancy. The standard deviation is calculated using an ASTROPY function known as `sigma_clipped_stats`. This function estimates the background noise in an image by iterating through the data and each time clipping values that deviate from the standard deviation by a factor of three. This is done until there is nothing left to clip; hence convergence has been achieved. `Sigma_clipped_stats` returns the standard deviation of the sigma-clipped image for each channel, which is shown in figure 3.1, where the standard deviation is plotted against each channel's velocity offset from the reference velocity of 7338.9 $\mathrm{km\,s^{-1}}$, calculated using the redshift of NGC 6240. This is shown for all three cubes with ROBUST values of -1.2, 0.0 and 0.5.

Moving forward, we assume one value for the standard deviation for each cube, represented by σ. This was calculated using the average standard deviation between the channels where H I emission appears, corresponding to recession velocities of 6890 $\mathrm{km\,s^{-1}}$ and 7538 $\mathrm{km\,s^{-1}}$, represented by the two vertical black lines in figure 3.1. The σ values for each cube are shown in table 3.1.

An example channel map from the cube with ROBUST = 0.5 is shown in the top-left panel of figure 3.2. This channel corresponds to recession velocity, $V_r = 6982$ $\mathrm{km\,s^{-1}}$, where you can see the deep H I absorption in blue, surrounding the dual AGN, represented by the crosses, and H I emission in red south of the absorption.

These components can be better illustrated by limiting the colour scale. To visually isolate H I emission, the image colour scale is clipped below -3.5σ, as shown in the top right plot in figure 3.2. Similarly, to isolate H I absorption, the image colour scale is clipped above 3.5σ, as shown in the bottom left plot of figure 3.2. Different

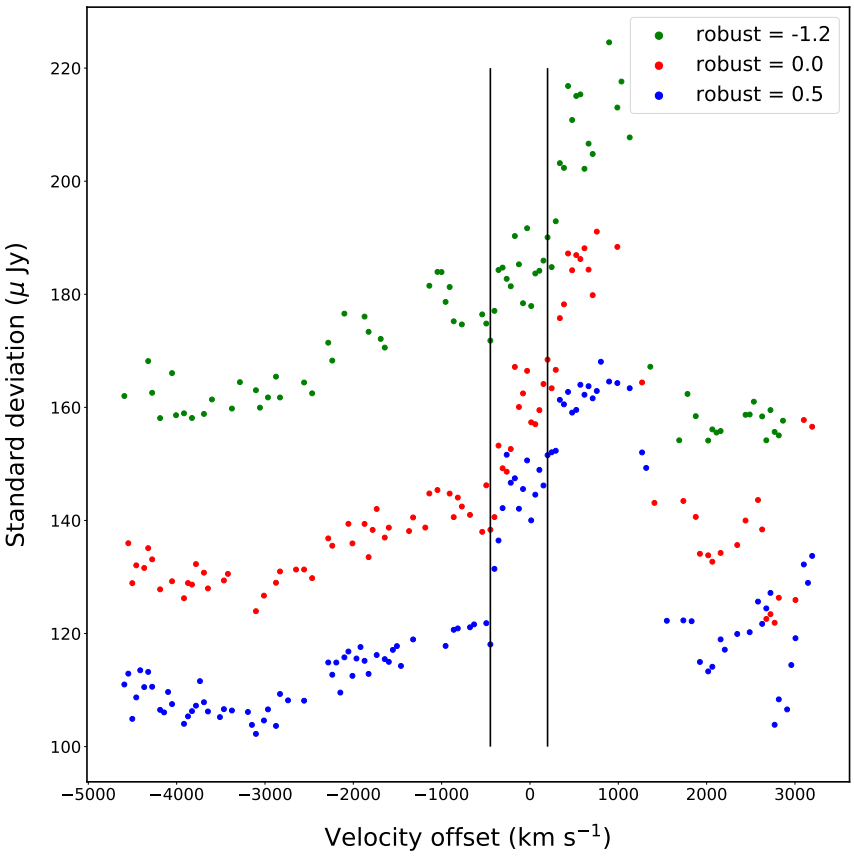

FIGURE 3.1: The standard deviation per channel for each cube. The average standard deviation value was calculated for each cube using values between 6890 km s^{-1} and 7538 km s^{-1} indicated by the black vertical lines. These channels were chosen as H I emission occurs at these velocities.

ROBUST	σ (μJy beam^{-1})	PSF FWHM	P.A.
0.5	145	22×12 arcsec^2	$-24°$
0.0	158	12×8 arcsec^2	$-26°$
-1.2	184	10×7 arcsec^2	$-24°$

TABLE 3.1: For each data cube with a different ROBUST value, the table shows the σ value calculated using the average standard deviation between channels with corresponding recession velocities of 6890 km s^{-1} and 7538 km s^{-1} as well as the point spread function full width at half maximum (PSF FWHM) and position angle (P.A.).

channels reveal different components of a source due to the different velocities. This is beneficial for a source, such as NGC 6240, which has many outflows and inflows (e.g. Müller-Sánchez et al. (2018) and Tacconi et al. (1999)).

The bottom right plot of figure 3.2 shows that the channel corresponding to recession velocity, $V = 7075$ km s^{-1}, revealing H I emission in a galaxy neighbouring NGC 6240, known as GALEXMSC J165300.69+022112.2.

The reason for showing the channel map examples is to show the quality of the data, continuum subtraction results and highlight the scientific richness of the spectral cube.

The continuum subtraction appears to have worked well with minimal artefacts. In the sub-cubes created to isolate NGC 6240 there appears to be emission that is not linked to any other part of the system and only appears in channel 85 and 86, corresponding to recession velocity 7492 km s^{-1} and 7445 km s^{-1}. This could be an example of an artefact from the continuum subtraction step or, more likely tidal debris from the galaxy merger.

There appears to be a loss of data quality with the channel corresponding to recession velocity, $V_r = 6752$ km s^{-1}. This could be due to radio frequency interference, RFI, possibly occurring at this frequency.

3.2 H I emission

3.2.1 Total H I intensity

MeerKAT's image fidelity and sensitivity enable H I emission to be mapped in NGC 6240 for the first time, despite many decades of study. The spectral line imaging also reveals H I emission in a neighbouring galaxy 90 kpc in projection from the centre of NGC 6240.

H I emission was isolated using a mask generated by clipping the flux below 3.5σ for each channel in each cube. The total intensity map, known as the moment 0 map, is created by integrating the intensity of each unmasked pixel over all selected frequency channels. This is given by,

$$\text{Integrated intensity} = \int S_v \, dv, \tag{3.1}$$

where S_v is the flux per pixel and v is the channel frequency (Meyer et al., 2017).

The moment 0 map of the line-only cube will locate where the H I gas is concentrated. Figure 3.3 shows the H I emission moment 0 maps created for each cube.

Moment 0 maps were created for flux less than -3.5σ to isolate H I absorption, shown by the blue contours in figure 3.3. There is deep absorption, with peak flux

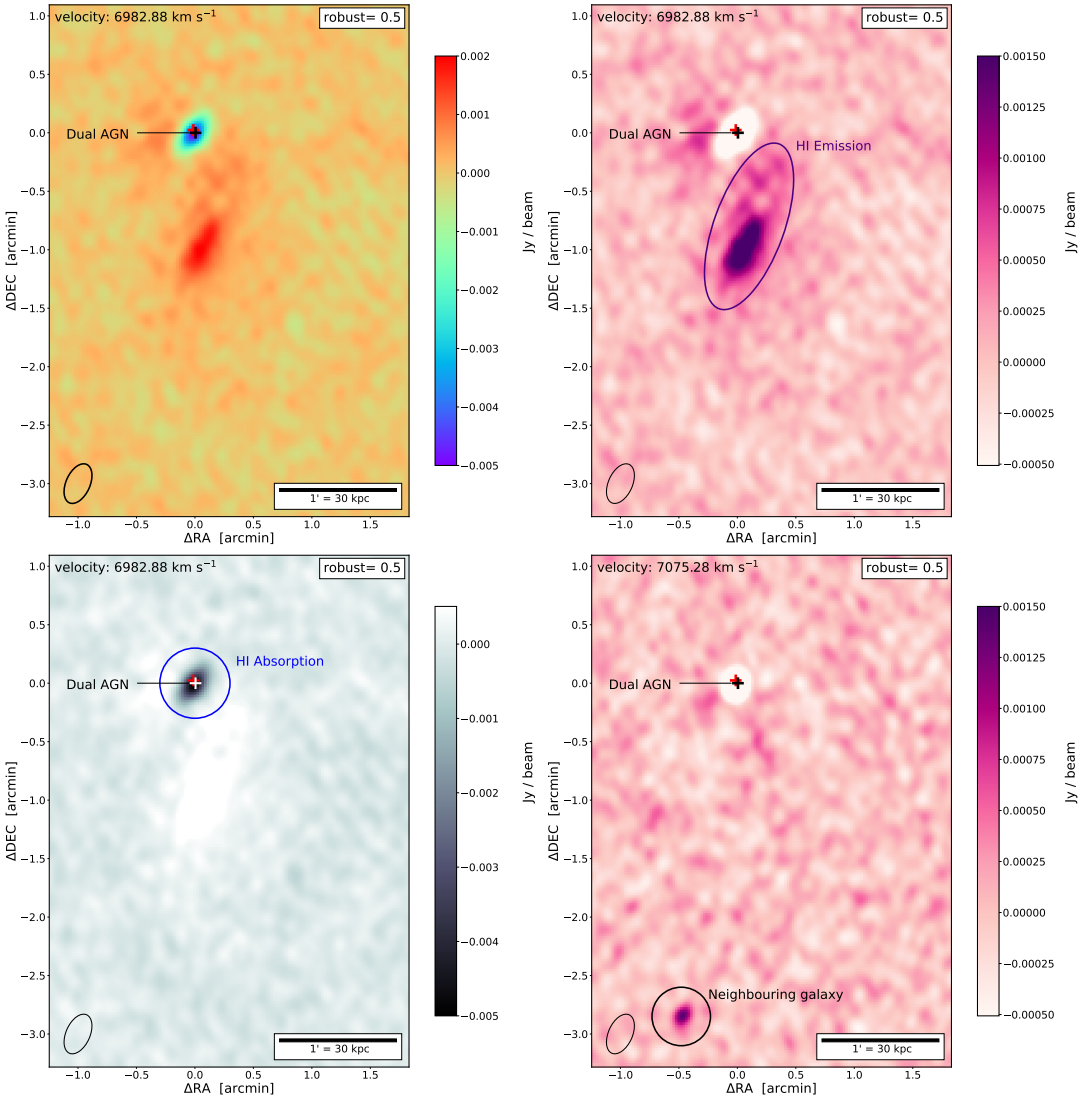

FIGURE 3.2: Channel maps created from the spectral line cube with ROBUST=0.5. Top left: the channel map corresponding to recession velocity $V_r = 6982$ km s^{-1}. Top right: same plot but with the colour scale clipped below -3.5σ, revealing H I emission. Bottom left: same channel map with colour scale clipped above 3.5σ revealing only H I absorption. Bottom right: Channel map with a recession velocity of 7075 km s^{-1} and colour scale clipped below -3.5σ revealing H I emission in the neighbouring galaxy, GALEXMSC J165300.69+022112.2.

per channel ranging from -5 mJy to -25 mJy. The red and black crosses show the dual AGN at the centre of NGC 6240. The southern-most H I component is a neighbouring galaxy with its spectroscopic redshift being measured for the first time. The black contours indicate the H I column density.

The moment 0 map for cube with ROBUST value of 0.5 shows more extended H I emission, figure 3.3a. This is expected for higher ROBUST values as it has higher sensitivity, as discussed in Chapter 2.

The H I emission morphology appears disrupted and one-sided predominantly toward the south of the two nuclei and H I absorption feature. There are two clear planes of H I emission; one aligns with the stellar disk and dust lane, referred to as the primary H I disk. The second H I plane is more diffuse and orientated towards the neighbouring galaxy, referred to as the south-east plane. The H I emission in the south-east plane extends out to $\sim$ 60 kpc. That, as well as the orientation and velocity, is strong evidence for ongoing interaction between NGC 6240 and the neighbouring H I galaxy, GALEXMSC J165300.69+022112.2, described in more detail in section 4.3.

In addition, there is a hint of H I tidal debris towards the south-west. The orientation is consistent with the primary H I disk and hence could be remnants of a tidal tail, referred to as tidal debris hereafter.

The H I emission is later compared to an optical HST view of NGC 6240in figure 4.1.

3.2.2 H I kinematics

The intensity-weighted velocity (moment 1) map shows the kinematics of the H I emission. This intensity-weighted map is the integral across the pixel velocities and weighted by intensity as in the following equation

$$\text{intensity-weighted velocity} = \frac{\int \nu S d\nu}{\int S d\nu} \tag{3.2}$$

where S is the flux per pixel and ν channel frequency/velocity (Meyer et al., 2017).

To create the moment 1 maps, as seen in figure 3.4, flux below 3.5σ was masked in each channel, as done with the moment 0 maps to isolate H I emission. The moment 1 maps are plotted with their contours overlayed at levels of 50 $\mathrm{km\,s^{-1}}$ for better visualisation of the kinematics. The subtracted recession velocity, $V_\mathrm{r} = 7339\ \mathrm{km\,s^{-1}}$, was calculated using the assumed redshift previously discussed.

3.3 H I absorption

As reported previously by Baan, Hagiwara, and Hofner (2007), there is deep H I absorption associated with the central radio emission. The cube with ROBUST weighting of -1.2 was used for H I absorption analysis as this was found to be a reasonable trade-off between angular resolution ($\sim$ 5 arcsec) and imaging sensitivity, since this has a significantly higher signal-to-noise ratio (SNR) than the H I emission and is also considerably more compact.

We performed high precision relative astrometry of H I absorption components which was motivated by high SNR, high image fidelity, presence of dual AGN and interest in reconciling H I absorption and emission.

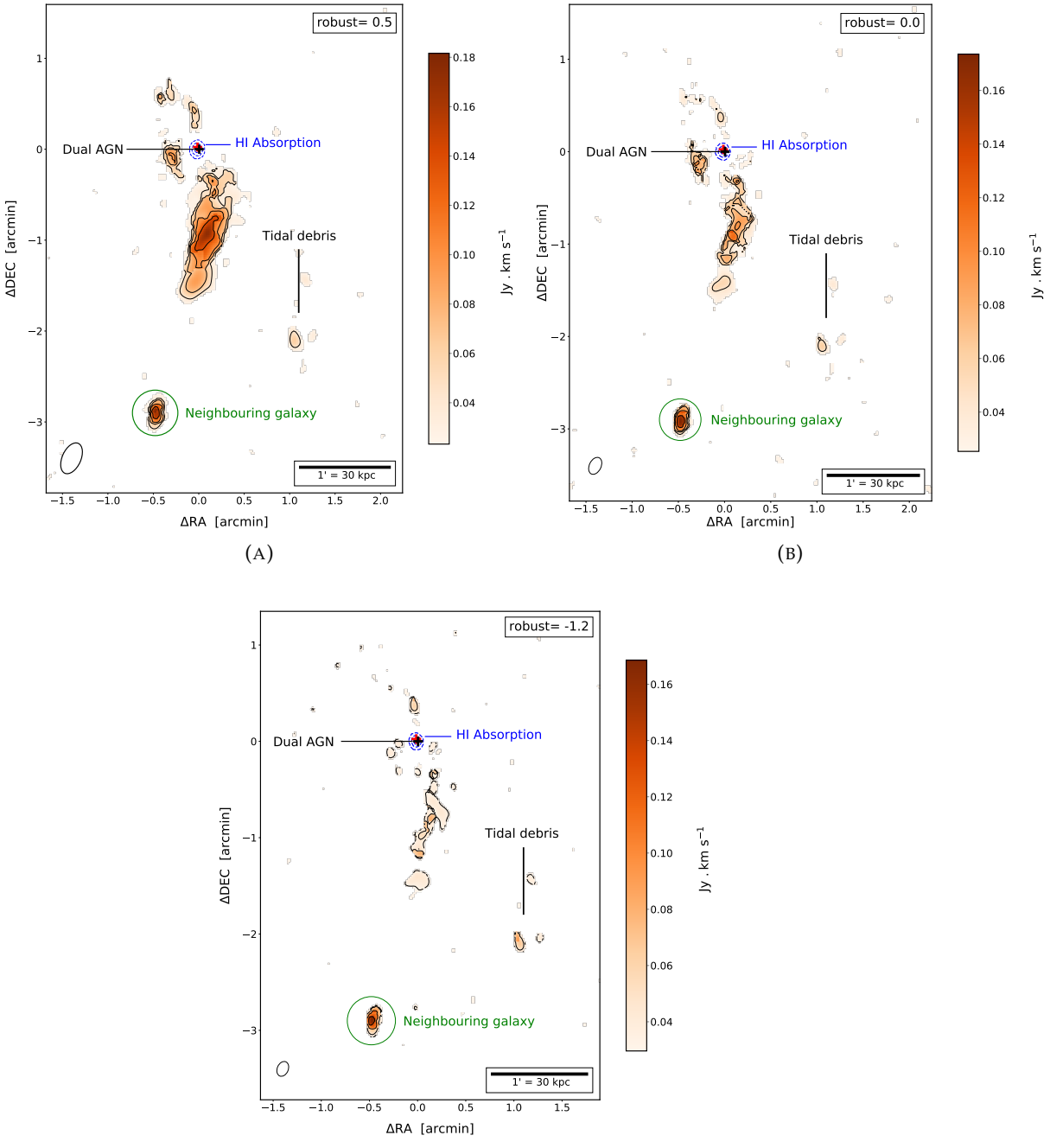

FIGURE 3.3: HI intensity maps (moment 0 maps) showing HI emission for each cube. Each cube was clipped below 3.5σ. The relevant parameters for each cube are listed in table 3.1. Panel (A) has HI column densities contour levels at $[3, 5, 7, 10]\times10^{20}$ cm^{-2}, panel (B) HI column densities at $[10, 15, 20, 30]\times10^{20}$ cm^{-2} and panel (C) HI column densities at $[7, 10, 20, 30]\times10^{20}$ cm^{-2}. The blue contours represent the velocity integrated intensity of HI absorption at levels [-9, -6, -3] Jy km s^{-1}. The red and black crosses indicated the location of the northern and southern nucleus, respectively. The neighbouring galaxy and tidal debris are labelled. The black ellipse in the bottom left corner of each map indicates the point spread function (PSF) for each cube.

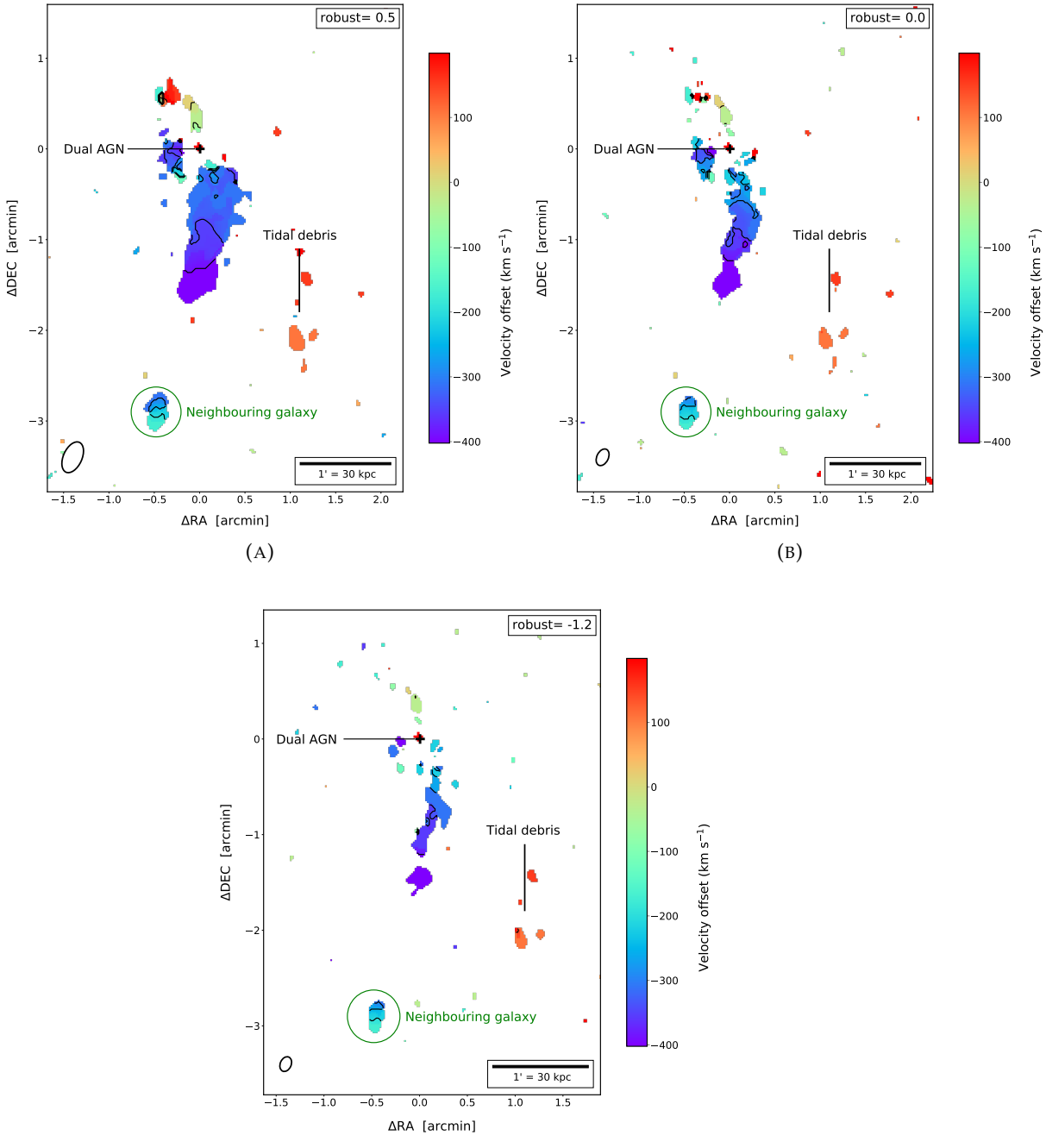

FIGURE 3.4: Velocity (moment 1) maps and contours showing H I emission kinematics for each cube extending from the centre of NGC 6240. Crosses indicate the location of the dual AGN. Panel (a) moment 1 map from cube with the ROBUST = 0.5, black contours increasing in steps of 50 km s^{-1}. Panel (b) moment 1 map from the cube with ROBUST = 0.0, black contours increasing in steps of 50 km s^{-1} and Panel (c) moment 1 map from the cube with ROBUST = -1.2, black contours increasing in steps of 50 km s^{-1}. The neighbouring galaxy and tidal debris are labelled. The black ellipse in the bottom left corner of each map indicates the point spread function (PSF) for each cube. The PSF dimensions are the same as quoted in Figure 3.3.

The absorption components were modelled by a single circular 2D Gaussian in each channel. The data were fit for pixels values less than 88 μJy beam^{-1} (0.5σ) to isolate the H I absorption. The single Gaussian fits appear to be a reasonable model for the data (see figure 3.5, 3.6, 3.7), therefore the residual cubes created represent the H I emission. Independent fits were made to each channel for which this converged. From the fit model, we obtained the peak absorption flux value of each fit per channel, along with the position of the peak and the uncertainties of these positions in RA and DEC.

Figure 3.8 compares the peak flux per channel for H I emission and absorption. For absorption, we see a clear dip around the central few channels and levels out as further away. The emission peak appears in approximately the same channels as the absorption profile, however, with an offset intensity-weighted centroid. The gradient of the H I absorption profile is shallower on the red wing. Therefore the absorption profile is asymmetric with a long blue-ward tail. When compared to the peak flux per channel for emission, we note that the profile peaks on the blue-ward region in H I absorption.

To investigate H I absorption further, the centroids of the Gaussian fit are plotted with the peak flux of H I absorption and H I emission per channel for NGC 6240, showing very deep absorption and peak emission around the central few channels. The two vertical lines enclose the channels where emission is observed, these channels have corresponding recession velocities between 6891 km s^{-1} (ΔV=-448 km s^{-1}) and 7724 km s^{-1} (ΔV=385 km s^{-1}), if we assume redshift of z=0.02448 from Downes, Solomon, and Radford (1993). The average channel noise rms is 0.2 mJy. The uncertainties of these positions in RA and DEC, are shown in figure 3.9. High dynamic range spectral line fitting imaging with MeerKAT enables this decoupling red-ward and blue-ward H I absorption components. This was done for the channels between the two vertical lines at ΔV_r = 6891 km s^{-1} and ΔV_r = 7724 km s^{-1} in figure 3.8. These channels were chosen as that is where H I emission is observed. The two black crosses in figure 3.9, represent the two nuclei. Tacconi et al. (1999) states that the major-axis of the CO disk has a P.A. of approximately 10-20° which is represented by the green region with a P.A. of 15°. The velocity profile of H I absorption has a similar orientation to the H I emission in the primary disk, as well as the approximate P.A. of the two nuclei and CO/dust plane.

A linear curve fit to the centroids in Figure 3.9 has a best-fit position angle of 28° $\pm$ 1.3°, where the uncertainty is calculated from the standard deviation of the residuals. This corresponds well to other gas and components in this system. Tacconi et al. (1999) states that the highly disturbed stellar disk structure has a P.A. of 25° east of north and Müller-Sánchez et al. (2018) states H_2 disk P.A. is 22°.

We also note hints of an arc-like structure in the H I absorption profile, similar to the radio continuum, as seen in Baan, Hagiwara, and Hofner (2007). However, this is for the lowest SNR channels, with correspondingly large uncertainties.

3.4 Derived H I properties

For each of the total intensity maps, we calculate the H I mass and H I column density, using equations from Meyer et al. (2017). The H I mass, M_{HI}, is given by,

$$\left(\frac{M_{HI}}{M_\odot}\right) \simeq \frac{2.35 \times 10^5}{(1+z)^2} \left(\frac{D_L}{\text{Mpc}}\right)^2 \left(\frac{S^{V_{obs}}}{\text{Jy km}s^{-1}}\right) \tag{3.3}$$

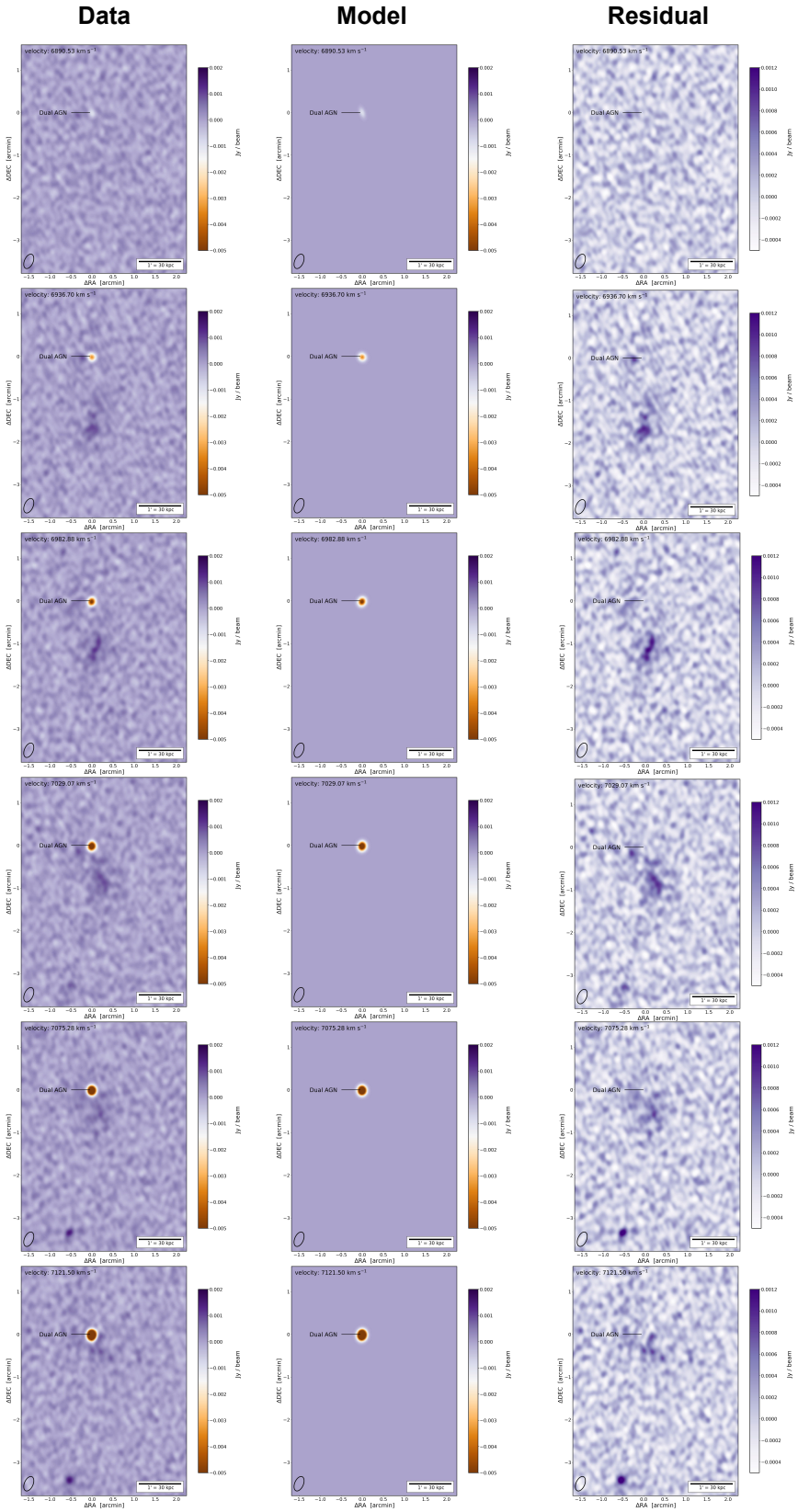

FIGURE 3.5: Cube with ROBUST = -1.2 channel maps for V_r = 6890.53 km s^{-1} to V_r = 7121.50 km s^{-1}. The left column is the original data from the cube. The middle column shows the single circular 2D Gaussian model for each channel for the absorption feature. The last column shows the residual data once this model has been subtracted from the original data, hence isolated H I emission.

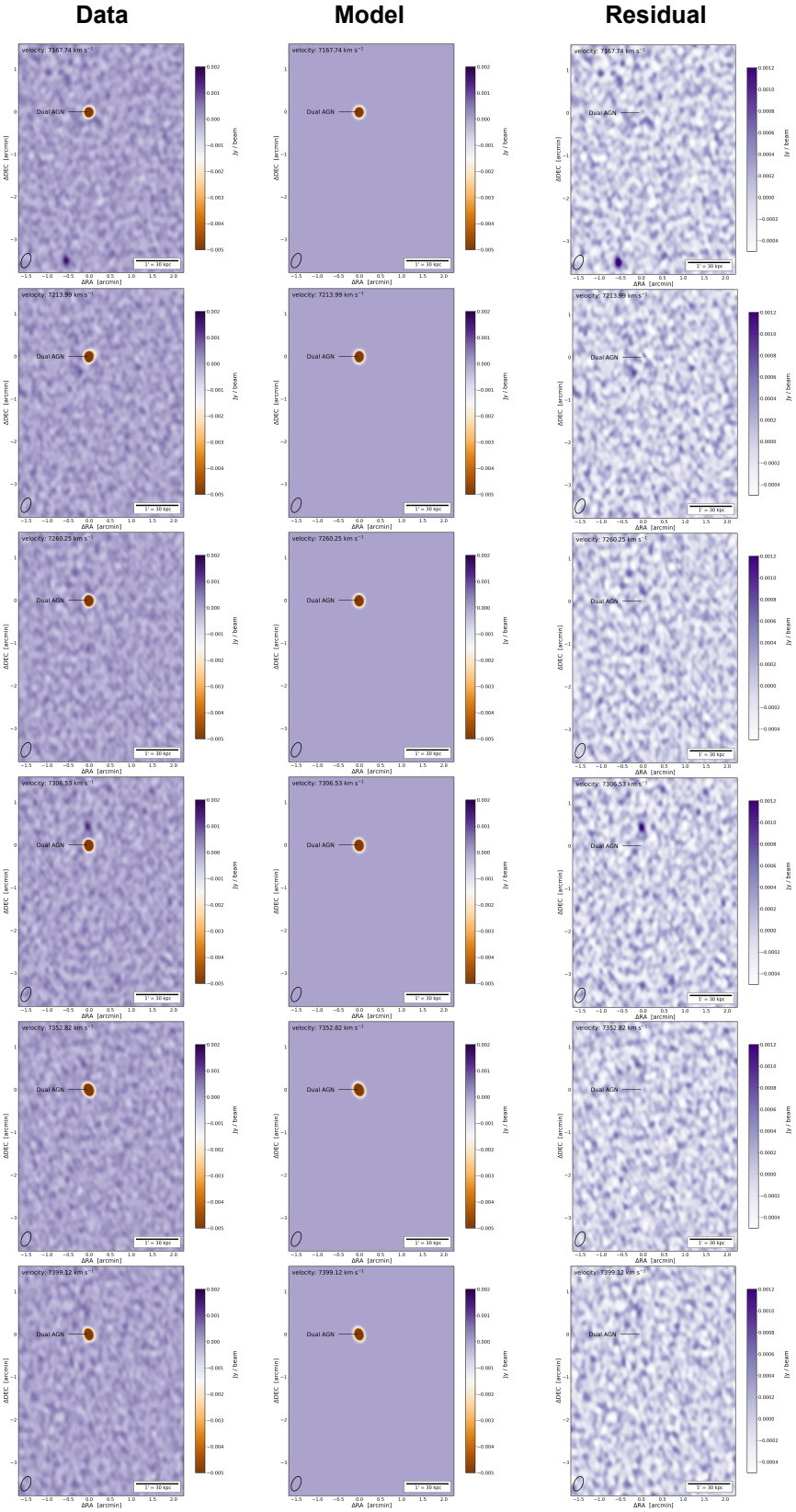

FIGURE 3.6: Continuation from figure 3.5 for channels $V_r = 7167.74$ km s^{-1} to $V_r = 7399.12$ km s^{-1}

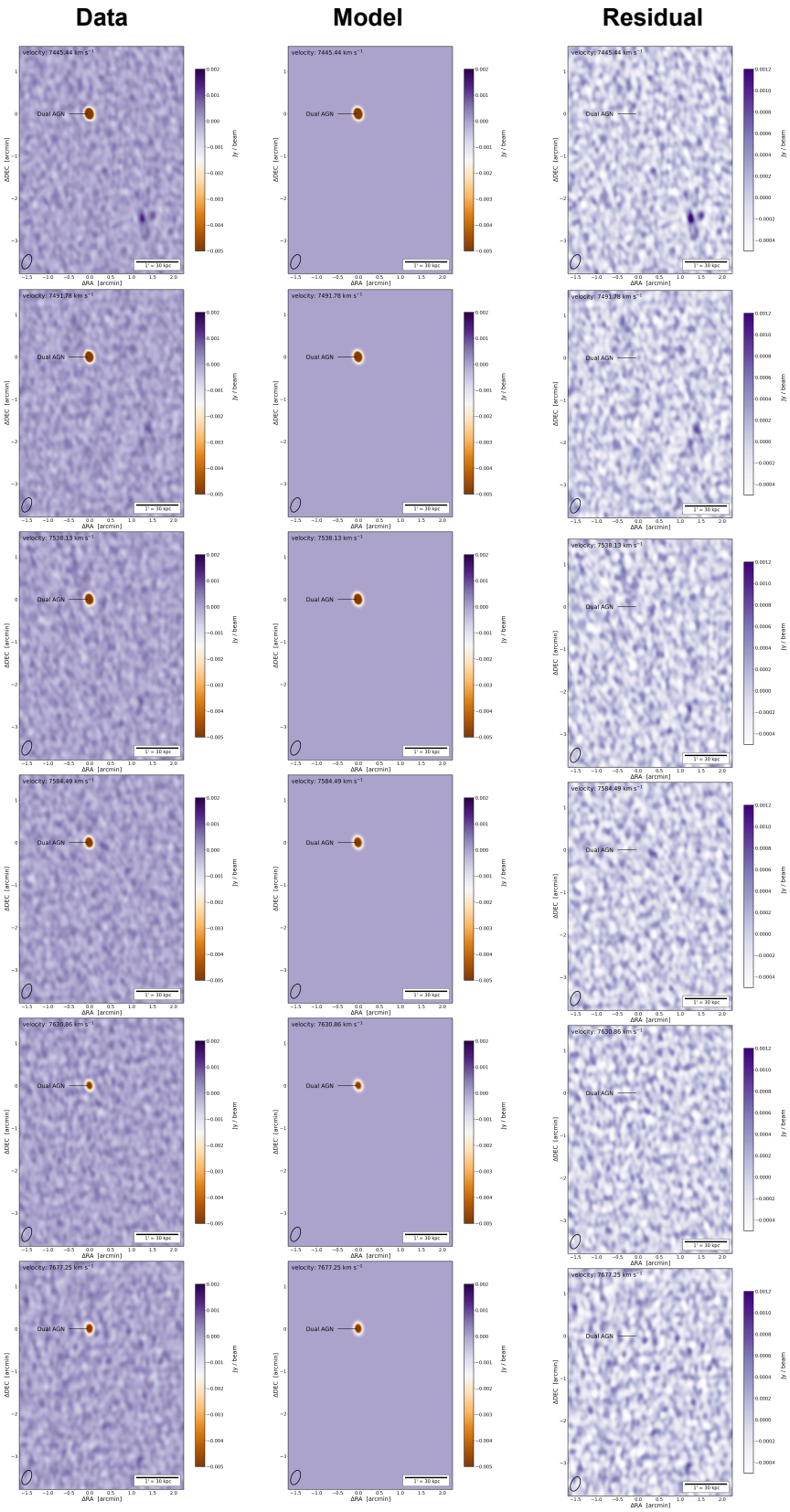

FIGURE 3.7: Continuation from figure 3.5 for channels $V_r = 7445.44$ km s^{-1} to $V_r = 7677.25$ km s^{-1}

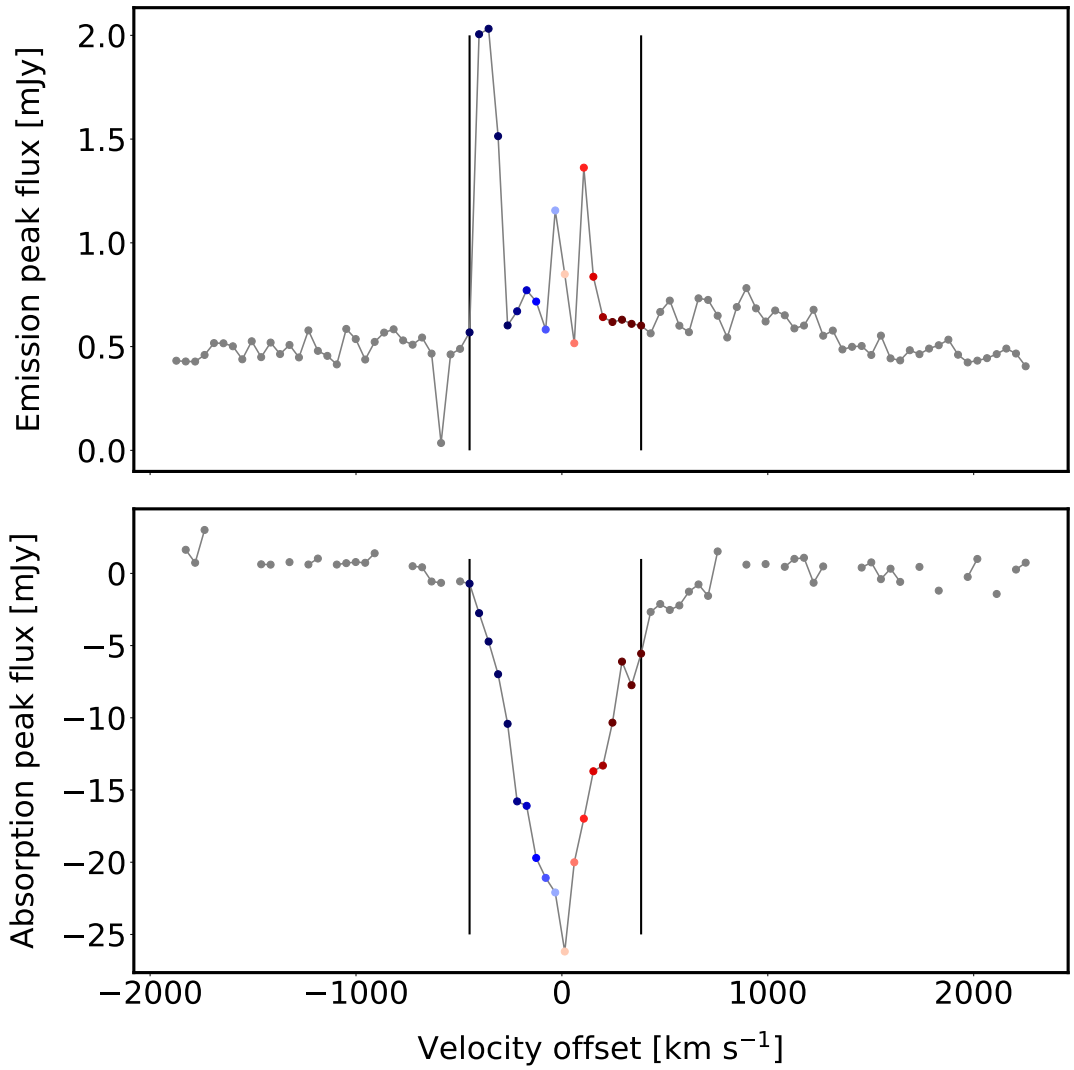

FIGURE 3.8: The peak flux of H I absorption and H I emission per channel for NGC 6240, showing very deep absorption and peak emission around the central few channels. The two vertical lines enclose the channels where emission is observed, these channels have corresponding recession velocities between 6891 km s^{-1} (ΔV = -448 km s^{-1}) and 7724 km s^{-1} (ΔV = 385 km s^{-1}) if we assume redshift of z=0.02448 from Downes, Solomon, and Radford (1993). The average channel noise rms is 0.2 mJy.

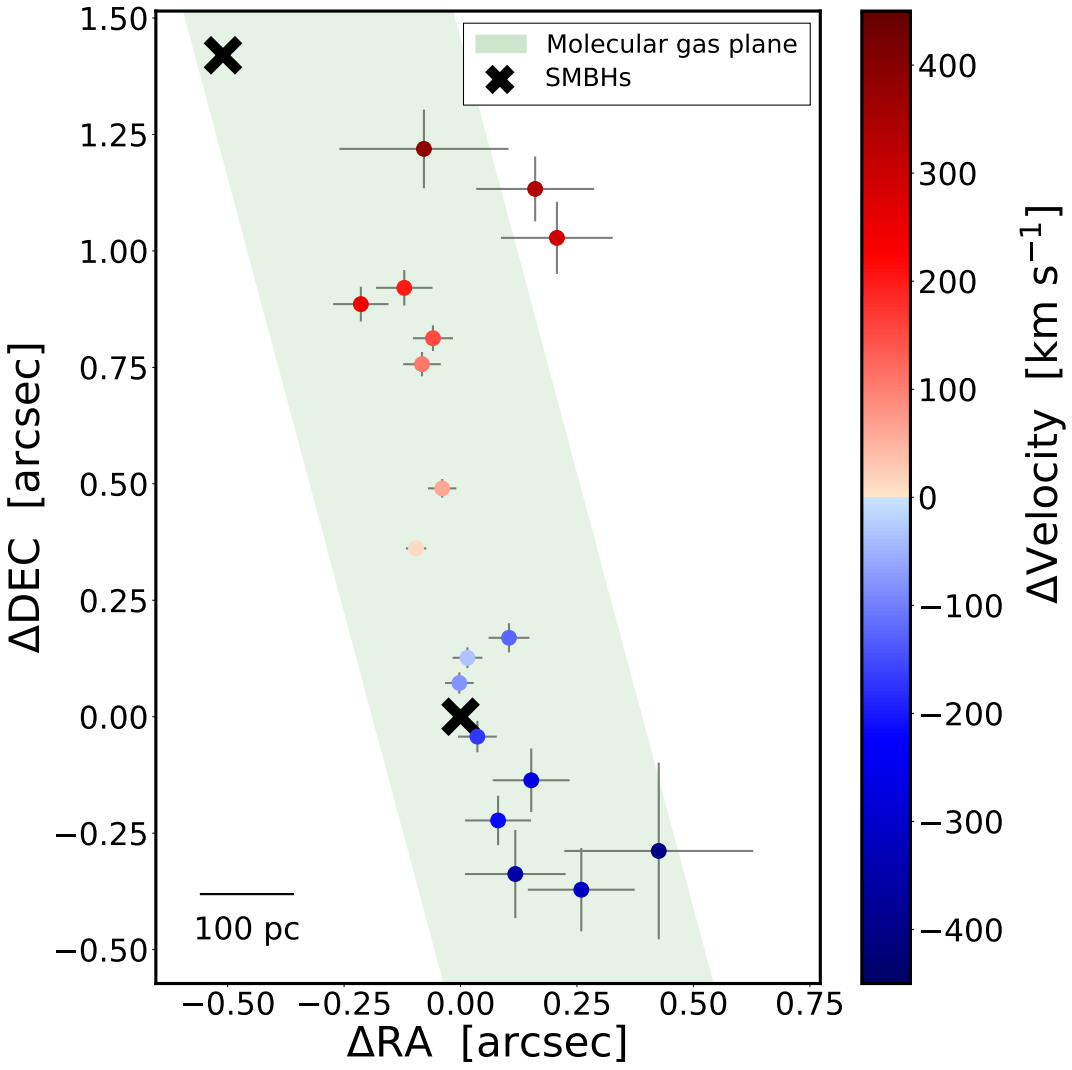

FIGURE 3.9: The centroid of 2D Gaussian fit to the H I absorption feature in 18 independent channels with associated fit uncertainties in RA and DEC. The black crosses represent the dual AGN and the green region at a P.A.=15°, is indicative of co-aligned CO(1 → 0) disk as measured in Tacconi et al. (1999).

Results Summary			
ROBUST	$M_{\rm HI}$ ($M_\odot$)	N_{HI}^{peak} (cm^{-2})	$\sigma_{N_{HI}}$ (cm^{-2})
0.5	1.6×10^9	1.3×10^{21}	0.6×10^{20}
0.0	2.3×10^9	3.8×10^{21}	2.3×10^{20}
-1.2	1.2×10^9	3.5×10^{21}	2.2×10^{20}

TABLE 3.2: This table summarises results from the derived H I properties for each cube of different ROBUST WEIGHTING. The properties displayed are H I mass ($M_{\rm HI}$), H I column density (N_{HI}^{peak}) and H I column density sensitivity ($\sigma_{N_{HI}}$).

where $S^{V_{obs}}$ is the observed-frame velocity-integrated flux and the luminosity distance $D_L = 110$ Mpc corresponding to $z = 0.02448$.

The H I column density is the number of neutral hydrogen atoms per unit area along the line of sight. This is given by,

$$\left(\frac{N_{HI}}{\rm cm^{-2}}\right) = 1.25 \times 10^{24}\ (1+z)^2 \left(\frac{\Omega_{\rm bm}}{\rm arcsec^2}\right)^{-1} \left(\frac{S^{V_{obs}}}{\rm Jy\ kms^{-1}}\right) \tag{3.4}$$

where $\Omega_{\rm bm}$ is the solid angle.

The rms of the column density, σ, are used in the column density sensitivity calculations. For this project, the column density sensitivity is quoted as 3σ. The σ values for each cube were calculated as described earlier in section 3.1. The column density sensitivity is calculated using the equation

$$\left(\frac{\sigma_{N_{HI}}}{\rm cm^{-2}}\right) = 2.64 \times 10^{20}\ (1+z)^4 \left(\frac{\Omega_{\rm bm}}{\rm arcsec^2}\right)^{-1} \left(\frac{3\sigma}{\rm Jy\ \ Hz}\right) \tag{3.5}$$

The column density sensitivity varies greatly with different ROBUST weighting. The higher the ROBUST value, the higher the sensitivity. This is shown in figure 3.10, where the column density sensitivity is plotted per channel for each data cube. The ROBUST=0.5 cube has a high column density sensitivity and hence is able to detect more diffuse emission.

Table 3.2 summarises these calculations, with H I mass, the peak of the column density and column density sensitivity (3σ).

The H I mass for ROBUST=0.0 is 2.3×10^9, the largest mass calculated for the three cubes. We expect the H I mass for the cube with larger ROBUST parameters, namely ROBUST=0.5, to be higher than the other cubes as it is sensitive to more diffuse H I emission. However, because the H I absorption region is only marginally resolved, it could be masking some of the H I emission in that region. This could explain why the cube of ROBUST 0.5 had a lower value H I mass but is more extended in the moment 0 map. Larger ROBUST values are ordinarily related to higher measured H I mass. However, larger PSF masks more H I emission by deep H I absorption, therefore lowering H I mass. To accurately calculate the H I mass for the cube with ROBUST 0.5 we would fit a 2D Gaussian on H I absorption region in the Fourier plane and subtract it from the data to get a more accurate measure of H I mass. However, this is beyond the scope of this master's project.

Using the H I mass calculated for the ROBUST 0.0 cube, we note that it is at the same order of magnitude as molecular gas mass, $M_{gas} \approx 2 - 4 \times 10^9\ M_\odot$, as calculated with multiple methods in Tacconi et al. (1999) using the CO emission, namely the CO J = 2→1 and CO 1→0 line. As expected, NGC 6240 is more gas-rich compared to typical galaxies, given its high star formation rate (e.g. Catinella et al.

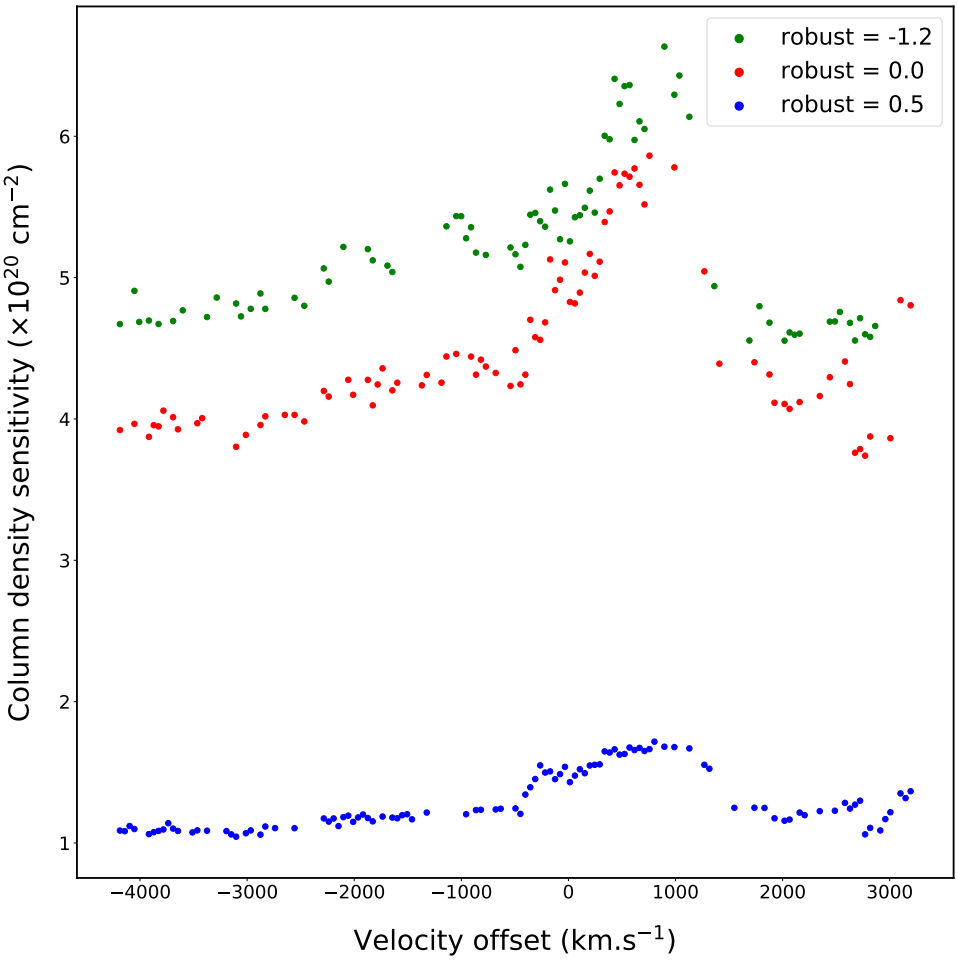

FIGURE 3.10: The column density (3σ) sensitivity per channel for each spectral line cube with ROBUST weightings of 0.5, 0.0 and -1.2. Cube with ROBUST=0.5 has the best column density sensitivity.

(2018) and references therein), this is discussed further in section 4.1. The H I mass of NGC 6240, $\log(M_{\rm HI}/M_\odot) = 9.36$, is comparable to the mass of our galaxy, the Milky Way. The knee of the $z = 0$ H I mass function derived in Jones et al. (2018), which corresponds to $\log(M_{\rm H\,I}/M_\odot) = 9.94$.

3.5 Multi-wavelength comparison

The H I results are now compared to the near ultraviolet (NUV) image of NGC 6240 from the *GALEX* space telescope in figure 3.11. The neighbouring galaxy has been detected in NUV, indicating that unobscured ongoing star formation has been triggered in the neighbouring galaxy. There is no NUV in the core of NGC 6240 but is obscured around the central few kpcs immediately surrounding the dual AGN. Figure 3.11 shows the H I emission for the cube with ROBUST=0.5 in black contours. From this we can see an anti-correlation between NUV and H I emission and absorption in NGC 6240.

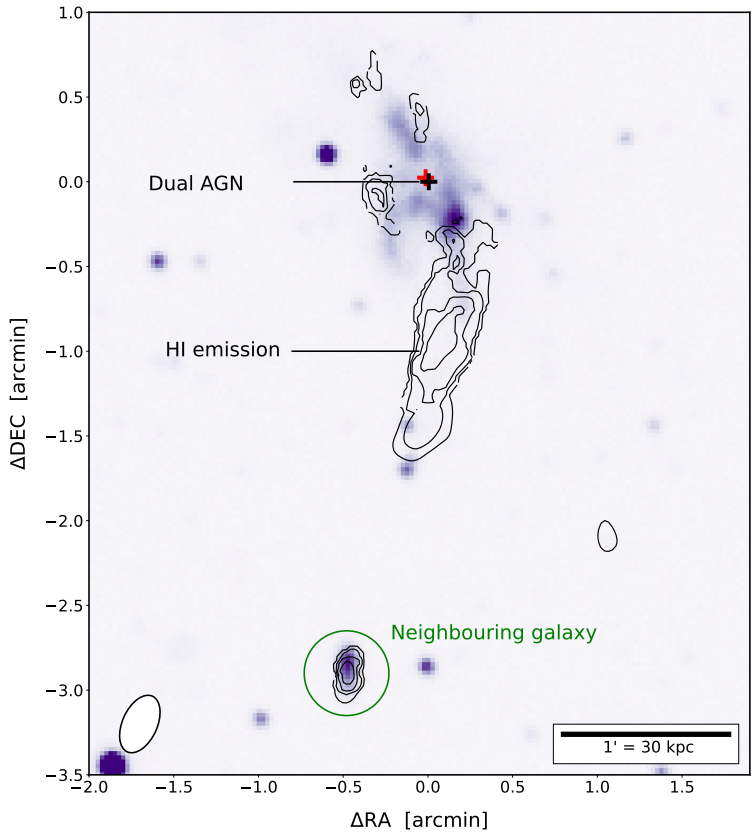

FIGURE 3.11: *Galex* near-ultraviolet (NUV) image of NGC 6240 in colour scale with black contour levels corresponding to H I column densities of $[3,5,7,10]\times10^{20}\,\mathrm{cm}^{-2}$, from the cube with ROBUST=0.5. NUV is seen in the neighbouring galaxy and surrounding nuclei of NGC 6240. The NUV indicates recent ($\lesssim$ 10 Myr) star formation. The neighbouring galaxy has been observed in x-rays with *Chandra*, which reveal an x-ray point source detection near its centre, presumably an AGN. Therefore indicating that the neighbouring galaxy has AGN activity.

When comparing the results to the x-ray image from *Chandra*[1], we found that the

[1]https://cxc.cfa.harvard.edu/csc/

x-ray emission is present in both NGC 6240 and the neighbouring galaxy. These x-ray observations indicate that there is AGN activity in NGC 6240 and the neighbouring galaxy. This is a clear early sign of interaction between NGC 6240 and the neighbouring galaxy, not evident through any other means. Interaction of the neighbouring galaxy with NGC 6240 has triggered the star formation found in the neighbouring galaxy. This neighbouring galaxy appears at a velocity offset of 250 $\mathrm{km\,s^{-1}}$ from V_r, indicating that this galaxy is approximately at the same redshift of NGC 6240.

Chapter 4

Discussion

This chapter will discuss the results and bring them together to get a more complete picture of H I in NGC 6240. In section 4.1, we outline a new perspective of NGC 6240 through H I emission. Section 4.2 discusses the spatially and spectrally resolved H I emission and absorption components with their velocity structures and orientations in greater detail. We then discuss possible evidence of unseen interactions of NGC 6240 with a neighbouring galaxy in section 4.3. Overall, this shows that MeerKAT's H I imaging can reveal important insights into environment-driven galaxy evolution.

4.1 A new perspective on NGC 6240: H I emission

This is the first time H I emission has been detected in NGC 6240, following decades of study. We want to compare this H I emission to other gas outflows and inflows in the system. A summary of the gas outflows and inflows of NGC 6240 found in previous papers are displayed in figure 4.1, along with the H I gas discussed in this project.

The H I absorption covers a compact circular region with a diameter of ~ 11 kpc from the centre of the dual AGN in our observation of NGC 6240. This region is the centre of the AGN-driven and starburst-driven outflow of ionized gas discussed in Müller-Sánchez et al. (2018), which extends out to 3.7 kpc and 90 kpc respectively. The arrows in figure 4.1 do not show the scale of these outflows and absorption feature but rather just the orientation of these previously-identified components (Baan, Hagiwara, and Hofner, 2007). The white contours show the H I emission intensity (moment 0) map from the cube with ROBUST weighting 0.5. The contours represent the H I column density at levels $[3, 5, 7, 10] \times 10^{20}\,\mathrm{cm}^{-2}$.

There is a clear asymmetry in the H I emission. In the northern/central region, it is disk-like, has the same orientation as and is aligned with the galactic dust plane. We refer to this as the primary H I disk. There are some differences between primary galactic disk and H I emission disk. First, the centroid of the molecular, stellar and dust emission is centred on the dual AGN, where as the centroid of the HI emission is south of the dual AGN. The H I emission velocity width, ranges from $\sim 200 - 400\,\mathrm{km\,s}^{-1}$, is much more narrow than that of molecular gas. The H I emission extends out to approximately 30 kpc which is a much larger spatial extent than the molecular gas.

In the southern region, the H I emission is inline with a nearby neighbouring galaxy at a projected separation of 90 kpc. We refer to this orientation as the south-east plane. The blue rectangles in figure 4.1 show the orientation of the two H I emission planes. We find that the majority of the H I emission is south of the dual AGN, including some tidal debris to the south-west.

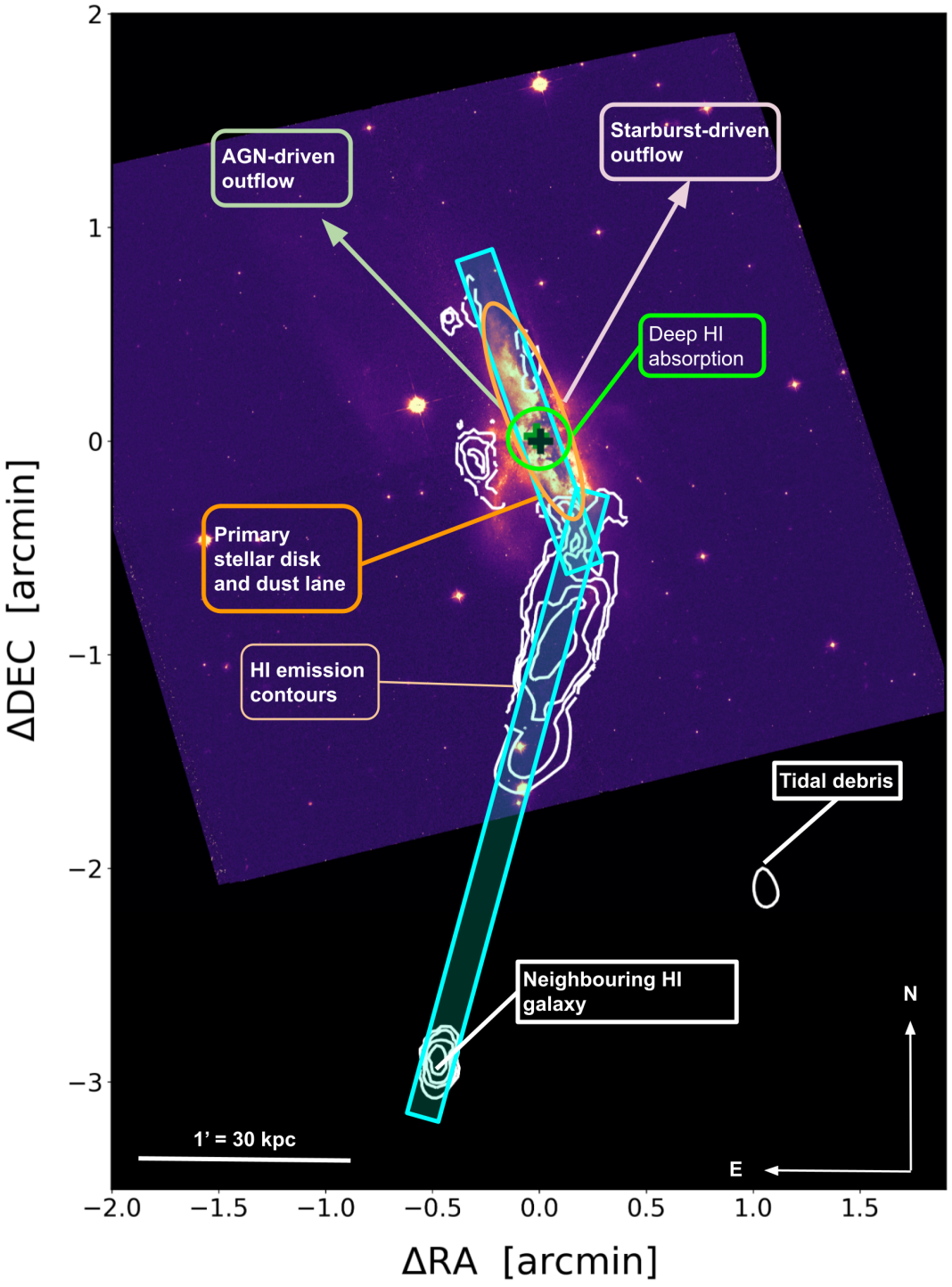

FIGURE 4.1: HST image of NGC 6240 using F435W filter (360-480 nm). H I emission column density contours levels at $[3, 5, 7, 10] \times 10^{20}$ cm^{-2}. This image shows other outflow directions given in a Nature paper by Müller-Sánchez et al. (2018) (not to scale), as well as the location of the neighbouring galaxy, tidal debris and H I absorption.

We calculate an H I mass of $M_{\rm H\,I} \sim 1.2 - 2.3 \times 10^9$ M$_\odot$, for a range of weighting schemes. The H I mass is the same order of magnitude of the molecular gas, $M_{gas} \sim 2 - 4 \times 10^9$ M$_\odot$, found in the highly turbulent central disk as discussed in Tacconi et al. (1999). When compared to the HIMF, we see that this mass is comparable to but just below the "knee" of the H I mass function at $z = 0$, which is log($M_{H\,i}/M_\odot$) = 9.9. NGC 6240 is more gas rich than other galaxies at this redshift, with a H I /H_2 ratio more typical of high redshift galaxies (Obreschkow and Rawlings, 2009).

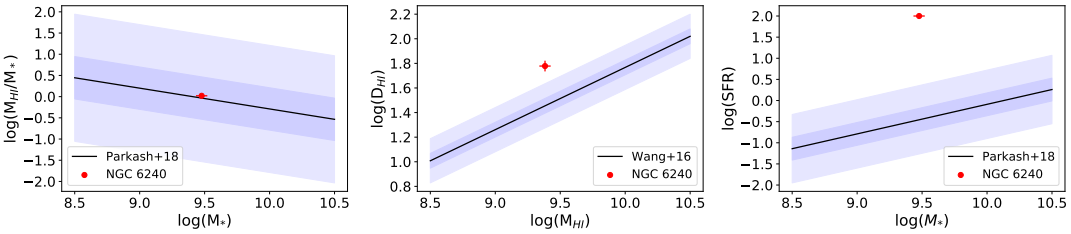

(A) (B) (C)

FIGURE 4.2: NGC 6240 deviation from scaling relations discussed in section 1.3.1. While not strictly applicable to a post-merger system, they serve as a useful comparison. The solid line shows the relation and the shaded regions are the 1σ and 3σ deviation for each. Panel A: NGC 6240 H I to stellar mass ratio is consistent with typical galaxies. Panel B: NGC 6240 diameter is 8σ off the relation where $\sigma = 0.06$ dex. Panel C: NGC 6240 SFR deviates by 9σ where $\sigma = 0.27$ dex

To investigate this further, we compare our system to other galaxies using the relations discussed in section 1.3.1. The H I mass and stellar mass fraction for NGC 6240, log($M_{\rm HI}/M_*$) = 0.02, is consistent with the H I gas fraction relation of galaxy sample from Parkash et al. (2018) (see figure 4.2a).

The H I extent of NGC 6240 is approximately 60 kpc (for the higher robust weightings) and is compared to the other nearby galaxies studied by Wang et al. (2016). The $D_{\rm H\,I}$-$M_{\rm H\,I}$ relation by Wang et al. (2016) is shown in figure 4.2b where the shaded region is the 1σ and 3σ deviation where $\sigma = 0.06$ dex. NGC 6240 H I diameter deviates by 8σ from this relation and hence has a significantly larger H I diameter when compared to other nearby galaxies. Of course, the Wang et al. (2016) study is of normal, non-interacting galaxies and this comparison is just to illustrate that the interaction has likely caused the measured H I extent to deviate from the typical relation.

Lastly we compare the SFR of NGC 6240, log(SFR)$\approx$ 2 (Müller-Sánchez et al., 2018). In the introduction chapter, we see from figure 1.4 that this SFR corresponds to a redshift of approximately 2. Compared to the galaxy sample from Parkash et al. (2018) in figure 4.2c, we see that it is 9σ above the relation, where σ=0.27 dex. Therefore the SFR of NGC 6240 is high in comparison to normal star formation galaxies.

Mergers with these parameters are typical at higher redshift ($z \sim 1 - 3$), but as we know, NGC 6240 is nearby, $z = 0.02448$. From these relations, it is possible that AGN and star formation have affected the H I gas fraction. Studying the H I details of nearby systems such as this will improve our understanding of the role H I plays in galaxy formation and evolution in systems at higher redshifts, where there is a drastic increase in merger rates.

4.2 Towards unifying the HI absorption and emission views of NGC 6240

H I in NGC 6240 is observed both in emission and absorption, which is rare. While the H I absorption has been studied in detail previously (Baan, Hagiwara, and Hofner, 2007), MeerKAT's high fidelity and dynamic range imaging allow us to perform high relative astrometry of the absorption, and place this in context with the newly-discovered H I emission presented in this work.

In figure 4.3, we compare the velocity profiles of both H I emission and the central H I absorption side-by-side. As previously discussed, the H I emission in the primary H I disk is at a position angle of 25° east of north. The mean H I velocity of this disk is shifted red-ward of the H I absorption (and quoted Solomon and Bout 2005 redshift typically used in the literature) by $\Delta 200$ km s^{-1}from the central velocity of NGC 6240, $\sim$ 7339 km s^{-1}. The H I absorption centroids form a quasi-linear structure with a similar position angle, PA=28°. The H I absorption components at the extreme blue and red end of the profile hint toward an arc-like structure seen in the radio continuum (e.g. Baan, Hagiwara, and Hofner, 2007), however, the uncertainties are comparable with the offset from a linear orientation. Overall, the velocity width of the H I absorption is approximately 800 km s^{-1}, consistent with the previous results, as well as the molecular gas in this system, and broader line widths seen in mergers in general.

The H I absorption is observed because there is high column density H I in front of the radio nuclei. At MeerKAT's $\sim$8 arcsec angular resolution (ROBUST -0.3), the H I absorption masks out some of the H I emission in the central region, influencing the H I mass calculated. We have attempted to account for this in the image-plane, however, decoupling H I emission from the H I absorption would be more accurately performed in the (u, v) domain using advanced modelling approaches, which are beyond the scope of this work.

The H I emission in the south-east plane is not orientated with H I absorption. The velocity width of the H I emission in this plane is $\sim$ 200 km s^{-1}, therefore H I in this direction has been influenced by an interaction with the neighbouring galaxy, changing its orientation and extent over time. Comparison with analogous systems in large-scale hydro-dynamical simulations may be a fruitful way to further this avenue of analysis.

Combining the H I absorption and emission, we are able to compare and contrast these two views and hence obtain a richer, more holistic picture of this prototypical merger system in the local-universe. At this point, there are consistencies (e.g. the inner gas orientation) and differences (e.g. the velocity widths and means). What is not clear at this point is if the H I absorption probes gas along the line-of-sight confined to the nuclear region, or if it further out. Either scenario presents interesting implications that are explored further in future work. Comparisons such as this will become increasingly important in detecting these components in future large sample pre-SKA and SKA surveys.

4.3 Evidence for a previously unseen galaxy interactions

We found that the orientation and velocity structure of the south-east plane is inline with a neighbouring galaxy, GALEXMSC J165300.69+022112.2, at a projected separation of $\sim$ 90 kpc and $\Delta V = 200$ km s^{-1}, meaning it lies within the full H I velocity width.

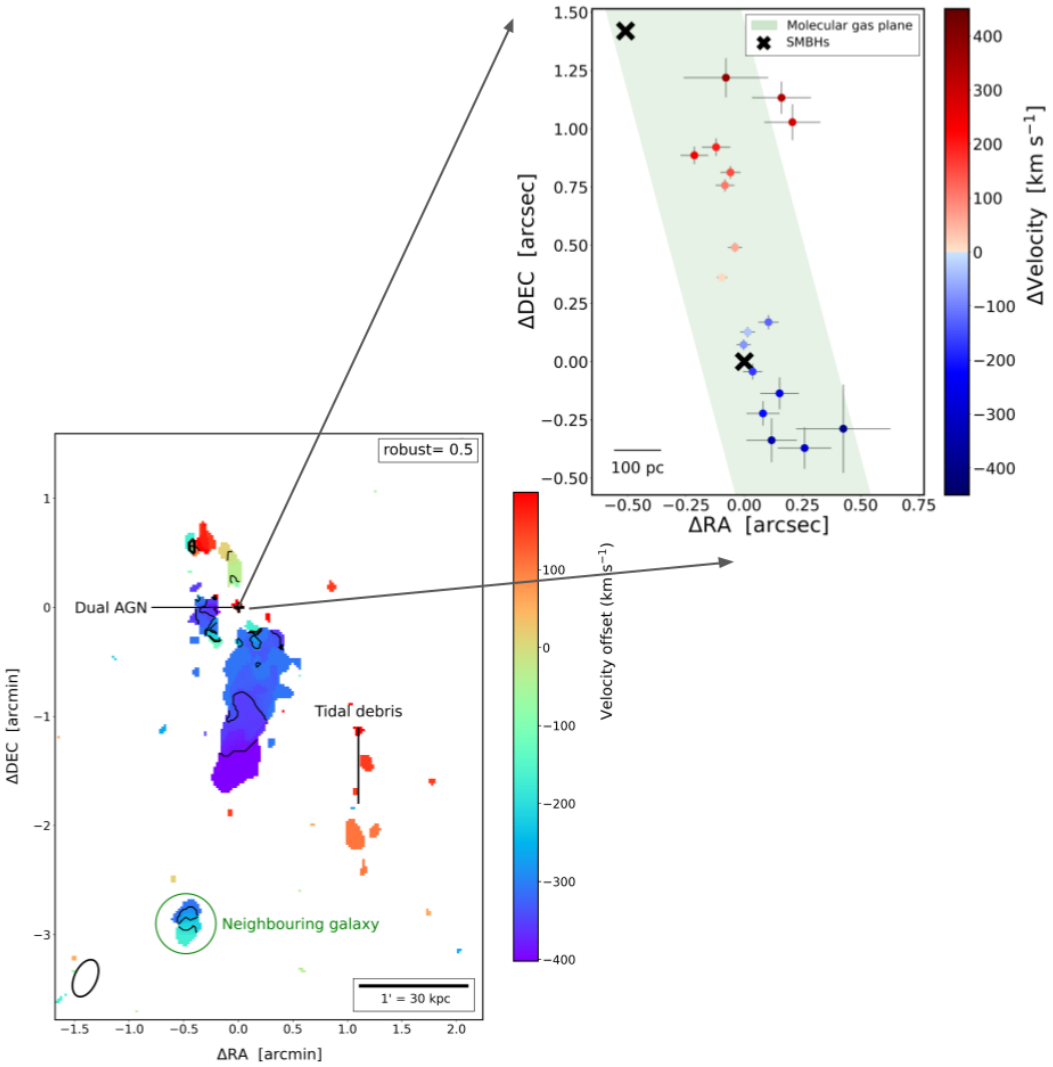

FIGURE 4.3: A comparison of the extended H I emission velocity structure with the central H I absorption velocity structure. Left: H I emission is shown by the intensity-weighted velocity map from the cube with ROBUST = 0.5, black contours increasing in steps of 50 km s^{-1}. Here we see an integrated velocity width of approximately 800 and 600 km s^{-1}for the H I absorption and emission, respectively. The H I emission velocity profile is dominated by the south-east plane, which spans approximately 100 km s^{-1}. Zooming in on the central region where the dual AGN are located, the right panel shows the centroid of 2D Gaussian fits to the H I absorption feature with the associated fit uncertainties. This shows a velocity profile qualitatively consistent with the H I emission velocity field.

The J2000 coordinates of this neighbouring galaxy are RA = 16h53m00.71s, DEC = +02d21m12.5s. The neighbour has an H I mass of 4.6×10^8 $M_\odot$, as well as active star formation and active nuclear black hole accretion indicated from the extended GALEX ultraviolet and compact Chandra x-ray emission[1], respectively. Therefore, both NGC 6240 and its neighbour have AGN and starburst activity, a scenario often seen of galaxy interactions (e.g. Hopkins et al. (2006a) and Mayer et al. (2007)). The dual AGN in the central $\sim$ 1 kpc of NGC 6240may not be the only cause of activity, some must be attributed to this larger-scale interaction.

As far as we know, this is the first evidence of interaction between NGC 6240 and this neighbouring galaxy. Therefore, the H I emission perspective offers a unique one, suggesting that the history of NGC 6240 is more complex than previously known. This is important insights into environmental-driven galaxy evolution enabled by high-fidelity H I spectral-line imaging with MeerKAT.

[1] https://cxc.cfa.harvard.edu/csc/

Chapter 5

Conclusions

In this thesis, we have presented MeerKAT spectral line observations of the archetype post-merger, dual AGN system NGC 6240. The high sensitivity and imaging fidelity of MeerKAT enabled us to observe H I emission in NGC 6240 for the first time, revealing new insights and perspectives on this well-studied merger system. The dataset is a challenging one in that it contains strong, extended continuum sources spread across the field, as well as deep H I absorption alongside H I emission. From our analysis, we present three primary new findings.

First, we find H I emission in two planes, one aligned with the primary galactic disk (primary H I disk) and the other is aligned with a neighbouring galaxy in the south-east direction with a projected separation of approximately 90 kpc from the NGC 6240 dual AGN. There is also evidence for some tidal debris in the south-west direction, which is in line with the primary H I disk but further out in its extent. The majority of the H I emission is found towards the south in the south-east plane extending out $\sim$ 60 kpc, which is opposite in direction to the x-ray emission extended in the north as discussed in Müller-Sánchez et al. (2018). The H I mass of this system is $\sim 2.3 \times 10^9$ $M_\odot$, placing it just below the knee of the local H I mass function. We find that NGC 6240 is an extremely neutral-hydrogen gas rich, high H I /H_2 ratio in comparison to typical star formation galaxies in the local universe, with a neutral-to-molecular gas as well as neutral-and-stellar mass ratios of order unity. The SFR of NGC 6240 is similar to the SFR in mergers found at $z = 2$.

Second, we measure the dynamics of the neutral gas probed by the H I absorption surrounding the dual AGN and along the line of sight. The relative astrometry of H I absorption components reveals a quasi-linear structure with a clear velocity gradient that is very similar in its orientation to the vector between the two AGN, the galaxy disk, and dust plane. We find that all the H I absorption centroids are within a $\sim$1.5 kpc region, similar to the projected separation of the two AGN. The H I absorption has a large velocity width of $\sim$ 800 km s^{-1}, as previously measured in earlier work. By comparing H I emission and absorption we find that there are some consistencies for example in the inner gas orientation, as well as differences such as velocity widths. The high relative astrometry could be performed due to the high SNR spectral line fitting imaging with MeerKAT, which allowed the decoupling of red-ward and blue-ward H I absorption components. This bodes well for similar MeerKAT observations and analyses on larger samples in the future. With both H I emission and H I absorption, we are able to compare and contrast the two views, providing a richer picture of this nearby prototypical galaxy merger.

Finally, MeerKAT detected a neighbouring H I galaxy in H I , GALEXMSC J165300.69 +022112, at a projected separation of $\sim$ 90 km s^{-1}. The H I extent, orientation change, and velocity overlap provide strong evidence that NGC 6240 and this neighbouring galaxy are interacting. This is shown here for the first time and is an integral part of the overall view of this systems. Extended ultraviolet emission and a nuclear

X-ray[1] point source in this neighbouring galaxy strongly argue that it contains active star formation and AGN activity which could have been triggered by this interaction. A more detailed investigation of this neighbouring system is the subject of future study.

Studying H I in detail in systems at low redshifts and comparing it to high redshift analogues, where there is a significant increase in galaxy merger rate, AGN prevalence and cosmic star formation. This will improve our understanding of H I and its role in galaxy formation and evolution because H I typically has a larger extent than optical and infrared components and can serve as a long timescale tracer of galaxy dynamics. Detailed studies with MeerKAT, such as this, may be an analogue for what SKA will do in the future.

[1] https://cxc.cfa.harvard.edu/csc/

Bibliography

Baan, Willem A, Yoshiaki Hagiwara, and Peter Hofner (2007). "Hi and oh absorption toward NGC 6240". In: *The Astrophysical Journal* 661.1, p. 173.

Blyth, Sarah Louise et al. (2016). "LADUMA: looking at the distant universe with the MeerKAT array". In: *Proceedings of Science*.

Broeils, Adrick H and M-H Rhee (1997). "Short 21-cm WSRT observations of spiral and irregular galaxies. HI properties." In: *Astronomy and Astrophysics* 324, pp. 877–887.

Bull, P et al. (2020). "Fundamental physics with the square kilometer array". In: *Publications of the Astronomical Society of Australia* 37.

Buta, Ronald J (2011). "Galaxy morphology". In: *arXiv preprint arXiv:1102.0550*.

Camilo, F et al. (2018). "Revival of the magnetar psr j1622–4950: Observations with meerkat, parkes, xmm-newton, swift, chandra, and nustar". In: *The Astrophysical Journal* 856.2, p. 180.

Catinella, Barbara et al. (2018). "xGASS: total cold gas scaling relations and molecular-to-atomic gas ratios of galaxies in the local Universe". In: *Monthly Notices of the Royal Astronomical Society* 476.1, pp. 875–895.

Condon, James J and Scott M Ransom (2016). *Essential radio astronomy*. Vol. 2. Princeton University Press.

Dale, James E (2015). "The modelling of feedback in star formation simulations". In: *New Astronomy Reviews* 68, pp. 1–33.

De Blok, WJG et al. (2017). "An overview of the MHONGOOSE survey: Observing nearby galaxies with MeerKAT". In: *arXiv preprint arXiv:1709.08458*.

Downes, DSPM, PM Solomon, and SJE Radford (1993). "Molecular gas mass and far-infrared emission from distant luminous galaxies". In: *The Astrophysical Journal* 414, pp. L13–L16.

Ewen, Harold Irving and Edward Mills Purcell (1951). "Observation of a Line in the Galactic Radio Spectrum: Radiation from Galactic Hydrogen at 1,420 Mc./sec." In: *Nature* 168.4270, pp. 356–356.

Giovanelli, Riccardo et al. (2005). "The arecibo legacy fast ALFA survey. I. Science goals, survey design, and strategy". In: *The astronomical journal* 130.6, p. 2598.

Glowacki, Marcin et al. (2022). "LADUMA: Discovery of a luminous OH megamaser at $z > 0.5$". In: *arXiv preprint arXiv:2204.02523*.

Gupta, Neeraj et al. (2017). "The MeerKAT absorption line survey (MALS)". In: *arXiv preprint arXiv:1708.07371*.

Haarlem, Michael P van et al. (2013). "LOFAR: The low-frequency array". In: *Astronomy & astrophysics* 556, A2.

Hagiwara, Yoshiaki, Willem A Baan, and Hans-Rainer Klöckner (2011). "Very long baseline interferometry observations of NGC 6240: Resolving the double nuclei and radio supernovae". In: *The Astronomical Journal* 142.1, p. 17.

Heckman, Timothy M and Philip N Best (2014). "The coevolution of galaxies and supermassive black holes: insights from surveys of the contemporary universe". In: *Annual Review of Astronomy and Astrophysics* 52, pp. 589–660.

Heywood, Ian (2020). "oxkat: Semi-automated imaging of MeerKAT observations". In: *Astrophysics Source Code Library*, ascl–2009.

Högbom, JA (1974). "Aperture synthesis with a non-regular distribution of interferometer baselines". In: *Astronomy and Astrophysics Supplement Series* 15, p. 417.

Hopkins, Philip F, Eliot Quataert, and Norman Murray (2012). "Stellar feedback in galaxies and the origin of galaxy-scale winds". In: *Monthly Notices of the Royal Astronomical Society* 421.4, pp. 3522–3537.

Hopkins, Philip F et al. (2006a). "A unified, merger-driven model of the origin of starbursts, quasars, the cosmic X-ray background, supermassive black holes, and galaxy spheroids". In: *The Astrophysical Journal Supplement Series* 163.1, p. 1.

Hopkins, Philip F et al. (2006b). "The relation between quasar and merging galaxy luminosity functions and the merger-driven star formation history of the universe". In: *The Astrophysical Journal* 652.2, p. 864.

Hopkins, Philip F et al. (2008). "A cosmological framework for the co-evolution of quasars, supermassive black holes, and elliptical galaxies. i. galaxy mergers and quasar activity". In: *The Astrophysical Journal Supplement Series* 175.2, p. 356.

Jansky, CM (1957). "The beginnings of radio astronomy". In: *American Scientist* 45.1, pp. 5–12.

Jarvis, Matt J et al. (2017). "The MeerKAT international GHz tiered extragalactic exploration (MIGHTEE) survey". In: *arXiv preprint arXiv:1709.01901*.

Jiang, Peng et al. (2019). "Commissioning progress of the FAST". In: *Science China Physics, Mechanics & Astronomy* 62.5, pp. 1–22.

Jonas, Justin and MeerKAT Team (2016). "The MeerKAT radio telescope". In: *MeerKAT Science: On the Pathway to the SKA*, p. 1.

Jones, Michael G et al. (2018). "The ALFALFA H i mass function: a dichotomy in the low-mass slope and a locally suppressed 'knee'mass". In: *Monthly Notices of the Royal Astronomical Society* 477.1, pp. 2–17.

Kleiner, D et al. (2021). "A MeerKAT view of pre-processing in the Fornax A group". In: *Astronomy & Astrophysics* 648, A32.

Komossa, Stefanie et al. (2002). "Discovery of a binary active galactic nucleus in the ultraluminous infrared galaxy NGC 6240 using Chandra". In: *The Astrophysical Journal Letters* 582.1, p. L15.

Lagos, Claudia del P, Sofía A Cora, and Nelson D Padilla (2008). "Effects of AGN feedback on ΛCDM galaxies". In: *Monthly Notices of the Royal Astronomical Society* 388.2, pp. 587–602.

Lazio, Joseph W et al. (2014). "Radio astronomy in LSST era". In: *Publications of the Astronomical Society of the Pacific* 126.936, pp. 196–209.

Loni, Alessandro (2022). "The low HI-mass galaxy population in the Fornax galaxy cluster". In:

Lotz, Jennifer M et al. (2011). "The major and minor galaxy merger rates at z< 1.5". In: *The Astrophysical Journal* 742.2, p. 103.

Maccagni, Filippo (2022). "Cold Gas Sustaining the Life-Cycle of AGNs". In: *Multiphase AGN Feeding & Feedback II*, p. 34.

Madau, Piero and Mark Dickinson (2014). "Cosmic star formation history". In: *arXiv preprint arXiv:1403.0007*.

Maina, EK et al. (2022). "Mapping H i 21-cm in the Klemola 31 group at z= 0.029: emission and absorption towards PKS 2020- 370". In: *Monthly Notices of the Royal Astronomical Society* 516.2, pp. 2050–2061.

Mayer, Lucio et al. (2007). "Rapid formation of supermassive black hole binaries in galaxy mergers with gas". In: *Science* 316.5833, pp. 1874–1877.

McMullin, Joseph P et al. (2007). "CASA architecture and applications". In: *Astronomical data analysis software and systems XVI*. Vol. 376, p. 127.

Meyer, Martin et al. (2017). "Tracing H i Beyond the Local Universe". In: *Publications of the Astronomical Society of Australia* 34.

Middelberg, Enno and Uwe Bach (2008). "High resolution radio astronomy using very long baseline interferometry". In: *Reports on Progress in Physics* 71.6, p. 066901.

Mo, Houjun, Frank C. van den Bosch, and Simon White (2010). *Galaxy Formation and Evolution*.

Morganti, Raffaella (2017). "The many routes to AGN feedback". In: *Frontiers in Astronomy and Space Sciences* 4, p. 42.

Morganti, Raffaella and Tom Oosterloo (2018). "The interstellar and circumnuclear medium of active nuclei traced by H i 21 cm absorption". In: *The Astronomy and Astrophysics Review* 26.1, pp. 1–59.

Morrissey, Patrick et al. (2007). "The calibration and data products of GALEX". In: *The Astrophysical Journal Supplement Series* 173.2, p. 682.

Müller-Sánchez, F et al. (2018). "Two separate outflows in the dual supermassive black hole system NGC 6240". In: *Nature* 556.7701, pp. 345–348.

Obreschkow, Danail and S Rawlings (2009). "THE COSMIC DECLINE IN THE H2/H i RATIO IN GALAXIES". In: *The Astrophysical Journal* 696.2, p. L129.

Offringa, AR et al. (2014). "WSCLEAN: an implementation of a fast, generic wide-field imager for radio astronomy". In: *Monthly Notices of the Royal Astronomical Society* 444.1, pp. 606–619.

Parkash, Vaishali et al. (2018). "Relationships between HI gas mass, stellar mass, and the star formation rate of HICAT+ WISE (H I-WISE) galaxies". In: *The Astrophysical Journal* 864.1, p. 40.

Péroux, Céline and J Christopher Howk (2020). "The Cosmic Baryon and Metal Cycles". In: *Annual Review of Astronomy and Astrophysics* 58, pp. 363–406.

Rodriguez-Gomez, Vicente et al. (2015). "The merger rate of galaxies in the Illustris simulation: a comparison with observations and semi-empirical models". In: *Monthly Notices of the Royal Astronomical Society* 449.1, pp. 49–64.

Schechter, Paul (1976). "An analytic expression for the luminosity function for galaxies." In: *The Astrophysical Journal* 203, pp. 297–306.

Sinigaglia, Francesco et al. (2022). "MIGHTEE-HI: Evolution of HI Scaling Relations of Star-forming Galaxies at z< 0.5". In: *The Astrophysical Journal Letters* 935.1, p. L13.

Solomon, PM and PA Bout (2005). "Molecular gas at high redshift". In: *arXiv preprint astro-ph/0508481*.

Stoehr, Felix et al. (2014). "The ALMA archive and its place in the astronomy of the future". In: *Observatory Operations: Strategies, Processes, and Systems V*. Vol. 9149. SPIE, pp. 17–25.

Strauss, Michael A et al. (2002). "Spectroscopic target selection in the Sloan Digital Sky Survey: the main galaxy sample". In: *The Astronomical Journal* 124.3, p. 1810.

Tacconi, LJ et al. (1999). "Gasdynamics in the luminous merger NGC 6240". In: *The Astrophysical Journal* 524.2, p. 732.

Thompson, A Richard, James M Moran, and George W Swenson (2017). *Interferometry and synthesis in radio astronomy*. Springer Nature.

Urry, C. Megan (2003). *AGN Unification: An Update*. arXiv: astro-ph/0312545 [astro-ph].

Wang, Jing et al. (2016). "New lessons from the H i size–mass relation of galaxies". In: *Monthly Notices of the Royal Astronomical Society* 460.2, pp. 2143–2151.